Dynamics of Gas and Dust in Protoplanetary Disks: Planet Formation From Observational and Numerical Perspectives

by

Jiaqing Bi
B.Sc., Xi'an Jiaotong University, China, 2018

A Thesis Submitted in Partial Fulfillment of the
Requirements for the Degree of

MASTER OF SCIENCE

in the Department of Physics and Astronomy

University of Victoria

Dynamics of Gas and Dust in Protoplanetary Disks: Planet Formation From Observational and Numerical Perspectives

by

Jiaqing Bi
B.Sc., Xi'an Jiaotong University, China, 2018

Supervisory Committee

Prof. Ruobing Dong, Supervisor
(Department of Physics and Astronomy)

Prof. Brenda Matthews, Departmental Member
(Department of Physics and Astronomy)

ABSTRACT

Dust and gas in protoplanetary disks are the building blocks of planets. In this thesis, we study the dynamics of the gas and dust, which are crucial for the planet formation theory, using observational and numerical approaches. The observational part contains the case study of a rare circumtriple disk around the GW Ori hierarchical triple system. We present Atacama Large Millimeter/submillimeter Array (ALMA) observations of 1.3 mm dust continuum and ^{12}CO $J = 2-1$ molecular gas emission of the disk. For the first time, we identify three dust rings in the GW Ori disk at $\sim$ 46, 188, and 338 au, with the outermost ring being the largest dust ring ever found in protoplanetary disks. We use visibility modeling of the dust continuum and kinematics modeling of CO lines to show that the disk has misaligned parts, and the innermost dust ring is eccentric. We interpret these substructures as evidence of ongoing dynamical interactions between the triple stars and the circumtriple disk. In the numerical part, we study whether or not dust around gas gaps opened by planets can remain settled by performing three-dimensional, dust-plus-gas simulations of protoplanetary disks with an embedded planet. We find planets that open gas gaps 'puff up' small, sub-mm-sized grains at the gap edges, where the dust scale-height can reach 80% of the gas scale-height. We attribute this dust 'puff-up' to the planet-induced meridional gas flows previously identified by Fung and Chiang. We thus emphasize the importance of explicit 3D simulations to obtain the vertical distribution of sub-mm-sized grains around planet gaps. We caution that the gas-gap-opening planet interpretation of well-defined dust rings is only self-consistent with large grains exceeding mm in size.

Contents

List of Tables

List of Figures

Acknowledgements

Foremost, I would like to express my sincere gratitude to my supervisor Prof. Ruobing Dong, for the continuous support of my study and research, and for his patience motivation, enthusiasm, and immense knowledge. I would like to thank Dr. Min-Kai Lin, Dr. Nienke van der Marel as well, who are the primary guiders of my research projects in this thesis. My sincere thankfulness also goes to Prof. Takayuki Muto and other co-authors in my journal publications, who offered a tremendous amount of support to make the work published.

Besides my collaborators, I would like thank Mr. and Ms. Boehm, Mr. and Ms. Hesser, and Mr. and Ms. Lipson, for their generous donations that supported my oversea conferences, workshops, and research collaborations.

Last but not the least, I would like to thank my family, who have unconditionally supported me throughout my life.

Chapter 1

Introduction

One of the most exciting developments in the field of planet formation is the direct observation of detailed sub-structures in protoplanetary disks (PPDs). The Atacama Large Millimeter/submillimeter Array (ALMA) has shown that many of the largest PPDs contain dust gaps and rings (Andrews et al. 2018; Long et al. 2018; van der Marel et al. 2019), while a smaller, but non-negligible fraction contain asymmetries such as lopsided dust clumps and spiral arms (e.g., van der Marel et al. 2013; Dong et al. 2018b).

The origin of these sub-structures is debated. For example, dust rings may be related to snow lines (Zhang et al. 2015; Pinilla et al. 2017; Hu et al. 2019), which can be sites of preferential planetesimal formation (Drążkowska and Alibert 2017). The rings may also result from pressure gradients. Solids in PPDs are subject to gas drag (Weidenschilling 1977), which causes their radial drift towards pressure maxima and expulsion by pressure minima (Whipple 1972). Axisymmetric pressure bumps can therefore act as dust traps to produce dust rings.

The planet interpretation of dust rings has become an attractive scenario as pressure bumps naturally arise from gap-opening by massive planets (Lin and Papaloizou 1993). Solids can then be trapped at the two gap edges on either side of the planet (Paardekooper and Mellema 2004, 2006; Rosotti et al. 2016; Dipierro and Laibe 2017; Weber et al. 2019; Meru et al. 2019; Yang and Zhu 2019). It is also possible for a single planet to open additional gaps away from its orbital radius (Bae et al. 2017) and thus produce more than two dust rings (Dong et al. 2017, 2018a). An accurate model of planet-induced dust rings can provide an indirect method to detect and characterize planets (as well as disk properties) during their formation (Lodato et al. 2019).

How are substructures like in PPDs around a multiple system, and how can they help to understand planet formation in multiple systems? In Chapter 2 we present high resolution ALMA observations in the disk around the GW Ori triple system at 1.3 mm dust continuum emission and ^{12}CO $J = 2 - 1$ emission, where we find three dust rings at $\sim$ 46, 188, and 338 au, with the outermost ring being the largest dust ring ever found in protoplanetary disks. We also show that the disk has misaligned parts, and the innermost dust ring is eccentric. Finally we suggest that the substructures hint at a companion at ~120 AU, which opens a deep gap and effectively breaks the gas disk at that radius.

Are sharp, flattened dust rings in sub-mm-sized grains observed in PPDs compatible with gas gaps opened by planets? To address this issue, we perform direct, grid-based simulations of 3D, dusty PPDs with embedded planets in Chapter 3. We find gas-gap-opening planets efficiently ‘puff-up’ sub-mm-sized dust grains around its gap edges, i.e., small grains do not settle. We attribute this to the planet-induced meridional gas flows identified by Fung and Chiang (2016). Our results suggest that 3D models of dusty gaps can be used to constrain the minimum grain size in well-defined, planet-induced dust rings in PPDs.

Chapter 2

GW Ori: Interactions Between a Triple-star System and its Circumtriple Disk in Action

GW Ori is a hierarchical triple system (Berger et al. 2011) at a distance of 402 ± 10 parsec (Gaia Collaboration et al. 2018). Two of the stars (GW Ori AB) compose a spectroscopic binary with a separation of ~ 1 AU (Mathieu et al. 1991). A tertiary component (GW Ori C) was detected by near-infrared interferometry at a projected distance of ~ 8 AU (Berger et al. 2011). The stellar masses have been constrained to be ~ 2.7, 1.7, and 0.9 $M_\odot$, respectively (Czekala et al. 2017). The system harbours a rare circumtriple disk, with dust extending to ~ 400 AU, and gas extending to ~ 1300 AU (Fang et al. 2017). Spectral energy distribution (SED) modelling indicates a gap in the disk at $25 - 55$ AU (Fang et al. 2014).

We arrange the chapter as follows: In Section 2.1, we describe the setups of the ALMA observations and data reduction. In Section 2.2, we present the imaged results of dust continuum and ^{12}CO $J = 2-1$ observations. In Section 2.3, we present results of dust continuum visibility modelling. In Section 2.4, we discuss the possible origins of the observed substructures. In Section 2.5, we summarize our findings and raise some open questions.

2.1 Observation and Data Reduction

The observations were taken on December 10, 2017 (ID: 2017.1.00286.S). The disk was observed in Band 6 (1.3 mm) by 46 antennas, with baseline lengths ranging from 15 to 3321 meters. The total on source integration time was 1.6 hours. There were two 1.875-GHz-wide basebands centered at 217 and 233 GHz for continuum emission, and three basebands with 117 MHz bandwidths and 112 kHz resolution, centered at 230.518, 219.541 and 220.380 GHz to cover the ^{12}CO, ^{13}CO and C^{18}O $J = 2-1$ lines.

The data were calibrated by the pipeline calibration script provided by ALMA. We used the Common Astronomy Software Applications package (CASA; version 5.1.1-5; McMullin et al. 2007) to process the data. We adopted CASA task CLEAN to image the continuum map (Figure 2.1a), with the UNIFORM weighting scheme and a 0".098 circular restoring beam. We performed phase self-calibration onto the image with a solution interval of 20 seconds. This resulted in an RMS noise level of ~ 40 μJy beam^{-1} and an enhanced peak signal-to-noise ratio (SNR) of ~ 157, compared with ~ 63 μJy beam^{-1} and ~ 90 before self-calibration, respectively. The integrated flux density of the disk (195 ± 20 mJy) is consistent with the result from previous ALMA observations (202 ± 20 mJy; Czekala et al. 2017).

The ^{12}CO $J = 2 - 1$ line data were obtained (after subtracting the continuum on the self-calibrated data) in the BRIGGS weighting scheme with robust = 0.5, and velocity resolution 0.5 km s^{-1}. The resulting line cube has a beam size of 0".122 × 0".159 at the position angle -32.3°. The noise level is ~ 1.4 mJy beam^{-1} per channel and the peak signal-to-noise ratio is ~ 83. Line emission was detected between 7.0 and 20.0 km s^{-1} with a central velocity of 13.5 km s^{-1}. The integrated flux is 60.6 Jy km s^{-1}, assuming a 2" radius. The intensity-weighted velocity map (a.k.a., the first-moment map) was constructed by calculating the intensity-weighted velocity with a threshold of three times the noise level. The averaged uncertainty of the twisted pattern in the first-moment map (i.e., the inset in Figure 2.1b) is ~ 0.2 km s^{-1}, derived from error propagation theory, assuming the uncertainty of velocity due to the channel resolution is 0.25 km s^{-1}. The observations of the CO isotopologues C^{18}O and ^{13}CO $J = 2 - 1$ emission will be presented in future work.

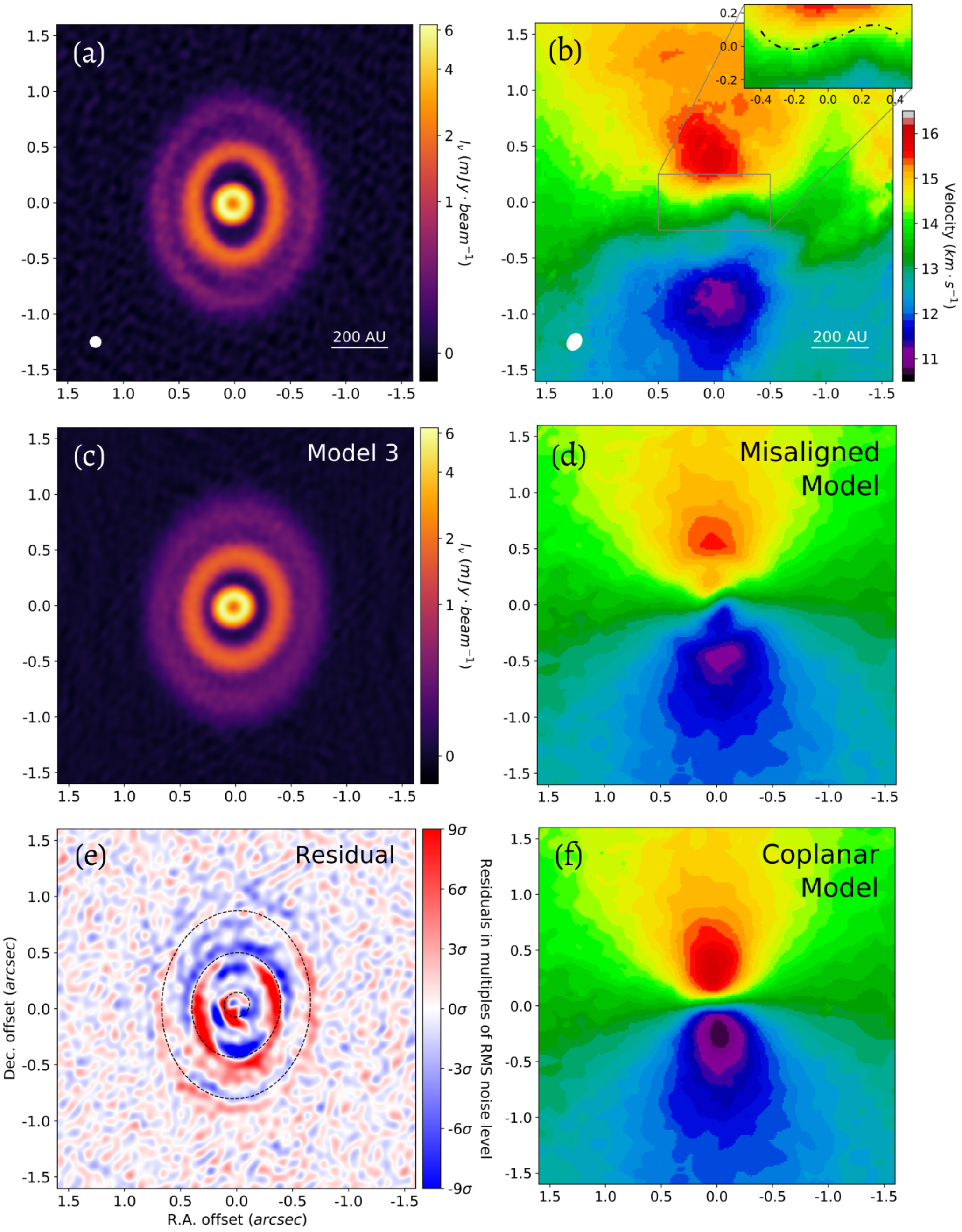

Figure 2.1: ALMA Observations and Models of the GW Ori disk. All panels are centered on the stellar position provided by GAIA DR2 (ICRS R.A. = $5^{\mathrm{h}}29^{\mathrm{m}}08^{\mathrm{s}}.390$ and Dec. = 11°52'12".661). (a): The ALMA self-calibrated dust continuum map performed with a 0".098 circular beam (bottom left corner; RMS noise level $\sigma \sim 40$ μJy beam^{-1}). (b): The ALMA ^{12}CO J=2-1 first-moment map performed with a 0".122 × 0".159 beam with a position angle of -32.3° (bottom left corner). The inset shows an 1" by 0".5 wide (40 by 20 AU) zoom, and the dot-dashed line highlights the shape of the twist. The averaged uncertainty in the inset region is $\sim$ 0.2 km s^{-1}. (c): Simulated ALMA continuum emission map of Model 3, produced in the same way as panel (a). (d): The synthetic first-moment map of the misaligned disk model, applying the model parameters listed in Table 2.2. The color scheme is the same as panel (b). (e): The residual map of Model 3. Dashed ellipses mark the fitted location of the three dust rings. The colorbar shows the residual magnitude in units of RMS noise level ($1\sigma = \sim 40$ μJy beam^{-1} $= \sim 0.6\%$ of peak surface density). (f): The synthetic first-moment map of the coplanar disk model, with an inclination of 37.9° and a position angle of -5° throughout the disk. The color scheme is the same as panel (b).

Table 2.1: The Complete MCMC Result of Dust Continuum Visibility Modelling

(a) Model 1

	Inner Ring	Middle Ring	Outer Ring
R.A Offset [$arcsecond$]	$1.89 \times 10^{-2}\,^{+9.47\times10^{-5}}_{-9.49\times10^{-5}}$	$-2.44 \times 10^{-3}\,^{+1.82\times10^{-4}}_{-2.08\times10^{-4}}$	$-4.24 \times 10^{-3}\,^{+4.64\times10^{-4}}_{-3.91\times10^{-4}}$
Dec. Offset [$arcsecond$]	$-1.32 \times 10^{-2}\,^{+1.09\times10^{-4}}_{-1.01\times10^{-4}}$	$-2.26 \times 10^{-2}\,^{+2.22\times10^{-4}}_{-2.06\times10^{-4}}$	$-1.21 \times 10^{-2}\,^{+6.57\times10^{-4}}_{-4.67\times10^{-4}}$
Ring Radius [$arcsecond$]	$1.15 \times 10^{-1}\,^{+1.46\times10^{-4}}_{-1.48\times10^{-4}}$	$4.68 \times 10^{-1}\,^{+3.07\times10^{-4}}_{-2.92\times10^{-4}}$	$8.40 \times 10^{-1}\,^{+1.03\times10^{-3}}_{-1.15\times10^{-3}}$
Ring Width [$arcsecond$]	$4.97 \times 10^{-2}\,^{+3.16\times10^{-4}}_{-6.24\times10^{-4}}$	$1.74 \times 10^{-1}\,^{+6.69\times10^{-4}}_{-7.56\times10^{-4}}$	$3.32 \times 10^{-1}\,^{+1.84\times10^{-3}}_{-2.78\times10^{-3}}$
Surface Brightness [$Jy/pixel$]	$2.49 \times 10^{-4}\,^{+1.80\times10^{-6}}_{-1.56\times10^{-6}}$	$3.96 \times 10^{-5}\,^{+8.67\times10^{-8}}_{-1.69\times10^{-7}}$	$1.13 \times 10^{-5}\,^{+2.77\times10^{-8}}_{-5.52\times10^{-7}}$
Inclination [$degree$]	$22.24\,^{+0.23}_{-0.31}$	$32.62\,^{+0.07}_{-0.11}$	$37.93\,^{+0.09}_{-0.08}$
Position Angle [$degree$]	$-60.75\,^{+1.06}_{-0.56}$	$-7.43\,^{+0.19}_{-0.12}$	$-3.57\,^{+0.15}_{-0.12}$

(a) Model 2

	Inner Ring	Middle Ring	Outer Ring
R.A Offset [$arcsecond$]		$1.77 \times 10^{-2}\,^{+1.69\times10^{-4}}_{-1.61\times10^{-4}}$	
Dec. Offset [$arcsecond$]		$-2.22 \times 10^{-2}\,^{+1.95\times10^{-4}}_{-1.99\times10^{-4}}$	
Ring Radius [$arcsecond$]	$1.17 \times 10^{-1}\,^{+1.36\times10^{-4}}_{-1.35\times10^{-4}}$	$4.68 \times 10^{-1}\,^{+2.88\times10^{-4}}_{-2.71\times10^{-4}}$	$8.40 \times 10^{-1}\,^{+9.48\times10^{-4}}_{-9.53\times10^{-4}}$
Ring Width [$arcsecond$]	$4.97 \times 10^{-2}\,^{+3.16\times10^{-4}}_{-3.91\times10^{-4}}$	$1.74 \times 10^{-1}\,^{+6.66\times10^{-4}}_{-6.03\times10^{-4}}$	$3.30 \times 10^{-1}\,^{+1.68\times10^{-3}}_{-1.96\times10^{-3}}$
Surface Brightness [$Jy/pixel$]	$2.51 \times 10^{-4}\,^{+1.53\times10^{-6}}_{-1.55\times10^{-6}}$	$3.96 \times 10^{-5}\,^{+8.20\times10^{-8}}_{-1.01\times10^{-7}}$	$1.13 \times 10^{-5}\,^{+2.65\times10^{-8}}_{-3.37\times10^{-8}}$

Inclination [*degree*]	$23.15^{+0.22}_{-0.23}$	$32.64^{+0.07}_{-0.07}$	$37.91^{+0.08}_{-0.07}$
Position Angle [*degree*]	$-55.67^{+0.61}_{-0.50}$	$-7.44^{+0.14}_{-0.12}$	$-3.60^{+0.13}_{-0.11}$
Apoapsis Angle [*degree*]	$65.04^{+0.50}_{-0.49}$	—	—
Eccentricity	$0.21^{+1.75\times10^{-3}}_{-1.43\times10^{-3}}$	—	—

(a) Model 3

	Inner Ring	Middle Ring	Outer Ring
Ring Radius [*arcsecond*]	$1.16 \times 10^{-1}\,^{+1.20\times10^{-4}}_{-1.49\times10^{-4}}$	$4.68 \times 10^{-1}\,^{+2.72\times10^{-4}}_{-2.98\times10^{-4}}$	$8.37 \times 10^{-1}\,^{+8.95\times10^{-4}}_{-1.06\times10^{-3}}$
Ring Width [*arcsecond*]	$4.99 \times 10^{-2}\,^{+3.06\times10^{-4}}_{-3.86\times10^{-4}}$	$1.73 \times 10^{-1}\,^{+6.33\times10^{-4}}_{-5.98\times10^{-4}}$	$3.39 \times 10^{-1}\,^{+1.90\times10^{-3}}_{-1.85\times10^{-3}}$
Surface Brightness [$Jy/pixel$]	$2.47 \times 10^{-4}\,^{+1.64\times10^{-6}}_{-1.42\times10^{-6}}$	$3.94 \times 10^{-5}\,^{+8.55\times10^{-8}}_{-1.12\times10^{-7}}$	$1.13 \times 10^{-5}\,^{+2.63\times10^{-8}}_{-3.33\times10^{-8}}$
Inclination [*degree*]	$20.63^{+0.23}_{-0.29}$	$32.86^{+0.06}_{-0.07}$	$37.96^{+0.09}_{-0.08}$
Position Angle [*degree*]	$-60.37^{+0.81}_{-0.65}$	$-7.26^{+0.13}_{-0.13}$	$-3.49^{+0.13}_{-0.12}$
Apoapsis Angle [*degree*]	$121.39^{+0.26}_{-0.25}$	—	—
Eccentricity	$0.19^{+8.55\times10^{-4}}_{-6.46\times10^{-4}}$	—	—

NOTE — The radius of each ring is the location of the peak in our model in Section 2.3, and the width is the full width at half maximum (FWHM) of the profile. The center offsets for Model 1 and Model 2 are relative to the center in Model 3, which is the location of GW Ori provided by GAIA DR2 (ICRS R.A. = $5^{\mathrm{h}}29^{\mathrm{m}}08^{\mathrm{s}}.390$ and Dec. = 11°52'12".661). The position angles and apoapsis angles are measured East of North. The inclination is defined in the range from 0° to 90°, with 0° denoting face-on. The pixel size in the unit of surface brightness is determined internally by GALARIO.

2.2 Observational Results

2.2.1 Dust Continuum Emission

Figure 2.1a shows the continuum map with spatial resolution of 0".098 (∼ 39 AU). We identify three dust rings with different apparent shapes in the disk at ∼ 46, 188, and 338 AU (hereafter the inner, middle, and outer ring). The location of the inner ring coincides with the predicted cavity size from SED modelling (Fang et al. 2017). The continuum flux densities of the inner, middle, and outer ring are 42 ± 4, 95 ± 10 and 58 ± 6 mJy, respectively. To our knowledge, the outer ring is the largest ever found in protoplanetary disks.

The three rings harbor an enormous amount of solid material. We estimate the dust (solid) mass $M_{\rm dust}$ of the rings with the equation provided in Hildebrand (1983)

$$M_{\rm dust} = \frac{F_\nu d^2}{B_\nu(T_{\rm dust})\kappa_\nu}, \tag{2.1}$$

where F_ν is the continuum surface brightness at a sub-mm frequency ν, d is the distance from the observer to the source, $B_\nu(T_{\rm dust})$ is the Planck function at the dust temperature $T_{\rm dust}$, and κ_ν is the dust opacity. The dust temperature is estimated using a fitting function provided by Dong et al. (2018c)

$$T_{\rm dust} = 30\left(\frac{L_\star}{38\,L_\odot}\right)^{1/4}\left(\frac{r}{100\,\mathrm{AU}}\right)^{-1/2}, \tag{2.2}$$

where $L_\star$ is the total stellar luminosity, and r is the location of the ring. The stellar luminosity modified by the distance provided by GAIA DR2 is 49.3 ± 7.4 $L_\odot$ (Calvet et al. 2004; Gaia Collaboration et al. 2018). We assume a dust grain opacity of 10 cm^2 g^{-1} at 1000 GHz with a power-law index of 1 (Beckwith et al. 1990). We estimate the dust masses of the rings to be 74 ± 8, 168 ± 19, and 245 ± 28 $M_\oplus$, respectively, with the uncertainties incorporating the uncertainties in the surface brightness of the rings, source distance, stellar luminosity, and radial location of the rings.

2.2.2 ^{12}CO J=2-1 Emission

Figure 2.1b shows the first-moment map of ^{12}CO $J = 2-1$ emission (with the zeroth-moment map provided in Appendix A.1). For regular Keplerian rotating disks, we expect a well-defined butterfly-like pattern in the first-moment map. However, we find a twisted pattern inside $\sim 0''.2$, which may result from a misalignment between the inner and outer parts of the disk (i.e., having different inclinations and orientations; Rosenfeld et al. 2014), as has been found in the disks around, e.g., HD 142527 (Casassus et al. 2015; Marino et al. 2015) and HD 143006 (Pérez et al. 2018; Benisty et al. 2018).

2.3 Modelling of Dust and Gas Emission

The different apparent shapes of the rings could result from a few scenarios, such as coplanar rings with different eccentricities, circular rings with different inclinations, or rings with both different eccentricities and inclinations. Here we present evidence for disk misalignment and disk eccentricity found in modelling the dust and gas emission.

2.3.1 Visibility Modelling of the Dust Continuum Emission

We fit the dust continuum map assuming that there are three dust rings in the disk with Gaussian radial profiles of surface brightness

$$F_i(r) = F_{0,i} \exp \frac{-(r - r_i)^2}{2\sigma_i^2}, \tag{2.3}$$

where F_i is the surface brightness as a function of the distance to the center r, with i = 1, 2, 3 denoting parameters for the inner, middle, and outer ring, respectively. $F_{0,i}$ is the peak surface brightness, r_i is the radius of the ring (i.e., where the ring has the highest surface brightness), and σ_i is the standard deviation.

Initially, we assume all three rings are intrinsically circular when viewed face-on, and their different apparent shapes entirely originate from different inclinations. For each ring, we assume an independent set of peak surface brightness, center location, radius, width, inclination, and position angle as the model parameters. We call this combination of assumptions Model 1.

After projecting the rings according to their position angles and inclinations, we calculate the synthetic visibility of the models using GALARIO (Tazzari et al. 2018), and launch MCMC parameter surveys to derive posterior distribution of model parameters using EMCEE (Foreman-Mackey et al. 2013). In the MCMC parameter surveys, the likelihood function L is defined as

$$\ln L = -\frac{1}{2}\sum_{j=1}^{N} m_j \times [(ReV_{\mathrm{obs},j} - ReV_{\mathrm{mod},j})^2 + (ImV_{\mathrm{obs},j} - ImV_{\mathrm{mod},j})^2] \tag{2.4}$$

where V_{obs} is the visibility data from ALMA observations, V_{mod} is the synthetic model visibility, N is the total number of visibility data points in V_{obs}, and m_j is the weight of each visibility data point in V_{obs}. The prior function is set to guarantee the surface brightness, ring radius, and ring width do not go below zero, the position angle does not go beyond (-90, 90) degrees, and the inclination does not go beyond (0, 90) degrees. For each model, there are 144 chains spread in the hyperspace of parameters. Each chain has 15000 iterations including 10000 burn-in iterations. The results of the parameter surveys are listed in Table 2.1.

The fitting result of Model 1, listed in Table 2.1a, suggests that the three rings have statistically different centers. Particularly, the center of the inner ring differs from the centers of the outer two by $\sim 20\%$ of the inner ring's radius. This non-concentricity indicates non-zero intrinsic eccentricities in the rings, particularly the inner ring (see Section 2.4.1).

We explore the non-zero intrinsic eccentricity in the inner ring with two models. In both models, the outer two rings are intrinsically circular and concentric. Their center coincides with one of the two foci of the inner ring. In Model 2, that center is set free, while in Model 3 it is assumed to coincide with the stellar position provided by GAIA DR2 (Gaia Collaboration et al. 2018). In those two models, we introduce two more parameters for the intrinsic eccentricity and apoapsis angle of the inner ring. The position angle only indicates the direction to the ascending node on the axis along which the ring is inclined. The fitting results are listed in Table 2.1b and 2.1c, and the following calculations are based on the result of Model 3.

Figure 2.1c and 2.1e show the model image and the residual map of Model 3, respectively. The residual map is produced by subtracting model from data in the visibility plane, and then imaging the results in the same way used for the observations. We interpret the residuals as additional substructures on top of the ideal model (e.g., a warp within the ring; Huang et al. 2020).

All three models yield roughly consistent inclinations and position angles of each ring. However, we cannot determine the mutual inclinations between them (i.e., the angles between their angular momentum vectors) from dust emission modelling alone,

Table 2.2: The Parameters Used in the Gas Kinematics Modelling

Inner Ring [*AU*]	Outer Ring [*AU*]	Longitude of the Ascending Node [*degree*]	Inclination [*degree*]
0	32	No Emission	
32	48	-60	22.3
48	153	-10	17.3
153	1000	-5	37.9

NOTE — The annuli are concentric with the center located at the stellar position provided by GAIA DR2 (ICRS R.A. = $5^{\rm h}29^{\rm m}08^{\rm s}.390$ and Dec. = 11°52'12".661). The longitude of the ascending node is measured East of North, and the inclination is defined in the range from 0° to 90° with 0° meaning face-on. The disk model is composed of an empty inner cavity and three annuli, inside out. The inner annulus (from 32 to 48 AU) is for the inner dust ring. The outer annulus (from 153 to 1000 AU) is for the middle and outer dust rings. The middle annulus (from 48 to 153 AU) is for the gap in between.

due to the unknown direction of orbital motion.

2.3.2 Kinematics Modelling of the ^{12}CO J=2-1 Emission

Following the prescription and parameter values used to fit low resolution CO isotopologue data of GW Ori (Fang et al. 2017), we set up a gas surface density model using a power-law profile with an exponential tail

$$\Sigma(r) = \Sigma_c \left(\frac{r}{r_c}\right)^{-\gamma} \exp\left[-(r-r_c)^{2-\gamma}\right], \tag{2.5}$$

and the aspect ratio h/r parametrized as

$$\frac{h}{r} = \left(\frac{h}{r}\right)_c \left(\frac{r}{r_c}\right)^{\psi}, \tag{2.6}$$

where Σ_c and $(h/r)_c$ are corresponding values at the characteristic scaling radius r_c. The disk mass is taken as 0.12 $M_\odot$, corresponding to $\Sigma_c = 3$ g cm^{-2} for $r_c = 320$ AU, with $\gamma = 1.0$, $(h/r)_c = 0.18$ and $\psi = 0.1$. The dust surface density profile is set by assuming a gas-to-dust ratio of 100, and decreasing the dust surface density by a factor of 1000 inside the derived gap radii: inside 37 AU, from 56 to 153 AU, and from 221 to 269 AU. The ^{12}CO channel maps are then computed and ray-traced by the physical-chemical modeling code DALI (Bruderer 2013), which simultaneously solves the heating-cooling balance of the gas and chemistry to determine the gas temperature, molecular abundances and molecular excitation for a given density structure.

Similar to Walsh et al. (2017), we model the misaligned disk with an inner cavity and three annuli each with its own inclination and position angle[1], as listed in Table 2.2. The channel map is run through the ALMA simulator using the settings of the ALMA observations. The resulting first-moment map is shown in Figure 2.1d. In Figure 2.1f we show the simulated first-moment map for another model as a comparison, in which the disk is coplanar with an inclination of 37.9° and a position angle of -5°.

The models show that the ^{12}CO $J = 2-1$ first-moment map in the ALMA observation cannot be reproduced by a coplanar disk. Instead, the misaligned disk model described in Table 2.2 matches the observed first-moment map better, indicating the presence of misalignment in the GW Ori disk.

2.4 Discussions

Several disks have been observed to have non-zero eccentricity and/or misalignment (e.g., MWC 758, Dong et al. 2018b; HD 142527, Casassus et al. 2015, Marino et al. 2015; and HD 143006, Pérez et al. 2018, Benisty et al. 2018). Unlike most of them, in which the origin is uncertain, the GW Ori system provides strong and direct link between substructures and star-disk gravitational interactions. Therefore it offers a unique laboratory to probe three-dimensional star-disk interactions. In this section, we discuss the possible origins of the observed substructures due to star-disk interactions.

2.4.1 Disk Eccentricity

The A-B binary and the C component can be dynamically viewed as an AB-C binary. The eccentricity of the circumbinary disk may increase through resonant interactions with the binary (Papaloizou et al. 2001). In the case of no binary-disk misalignment, the binary's perturbing gravitational potential on the midplane of the disk is given by Lubow (1991). The coupling of this perturbing potential with the imposed eccentricity

---

[1] DALI is unable to vary inclination as a function of radius. The final channel map is constructed by concatenating three channel maps, each for one component, ray-traced at its inclination and position angle and cut out at the specified radius range listed in Table 2.2.

of the disk excites density waves at the 1:3 outer eccentric Lindblad Resonance, which lead to angular momentum removal in the inner parts of the disk. As no energy is removed along with the angular momentum in this process, the disk orbit cannot remain circular (Papaloizou et al. 2001). In the case of GW Ori, the inner dust ring is the most susceptible to this effect, which could explain why its center in Model 1 is more deviated from those of the other two rings.

2.4.2 Binary-disk Misalignment

Our dust and gas observations alone cannot break the degeneracy in the mutual inclination between different parts in the disk due to the unknown on-sky projected orbital direction of the disk. Previous studies indicate that the on-sky projected gas motion is likely to be clockwise (Czekala et al. 2017), same as the orbital motion of GW Ori C given by astrometric observations (Berger et al. 2011). Given the inclination and longitude of ascending node of the AB-C binary orbit being 150 ± 7 and 282 ± 9 degrees (Czekala et al. 2017), we assume that the entire disk has the same clockwise on-sky projected orbital direction. Following Fekel (1981), we find out that the binary-disk misalignments at 46 AU (the inner ring), 100 AU (a gap), 188 AU (the middle ring), and 338 AU (outer ring) are 11 ± 6, ∼28[2], 35 ± 5, and 40 ± 5 degrees, respectively. A schematic diagram of our disk model is displayed in Figure 2.2. Therefore, the inner ring and the AB-C binary plane are close to being coplanar, and there is a monotonic trend of binary-disk misalignment from $\sim 10^\circ$ at $\sim$ 50 AU to $\sim 40^\circ$ at $\sim$ 340 AU, consistent with the expected outcome of the disk misalignment (see Section 2.4.3).

Several mechanisms could produce an initial binary-disk misalignment, such as turbulence in the star-forming gas clouds (Bate 2012), binary formation in the gas cloud whose physical axes are misaligned to the rotation axis (Bonnell and Bastien 1992), and accretion of cloud materials with misaligned angular momentum with respect to the binary after the binary formation (Bate 2018).

2.4.3 Misalignment Within the Disk

A test particle orbiting a binary on a misaligned orbit undergoes nodal precession due to gravitational perturbations from the binary (Nixon et al. 2011; Facchini et al.

---

[2] the manual fitting of gas model cannot provide any uncertainties for the gap between the inner and middle ring

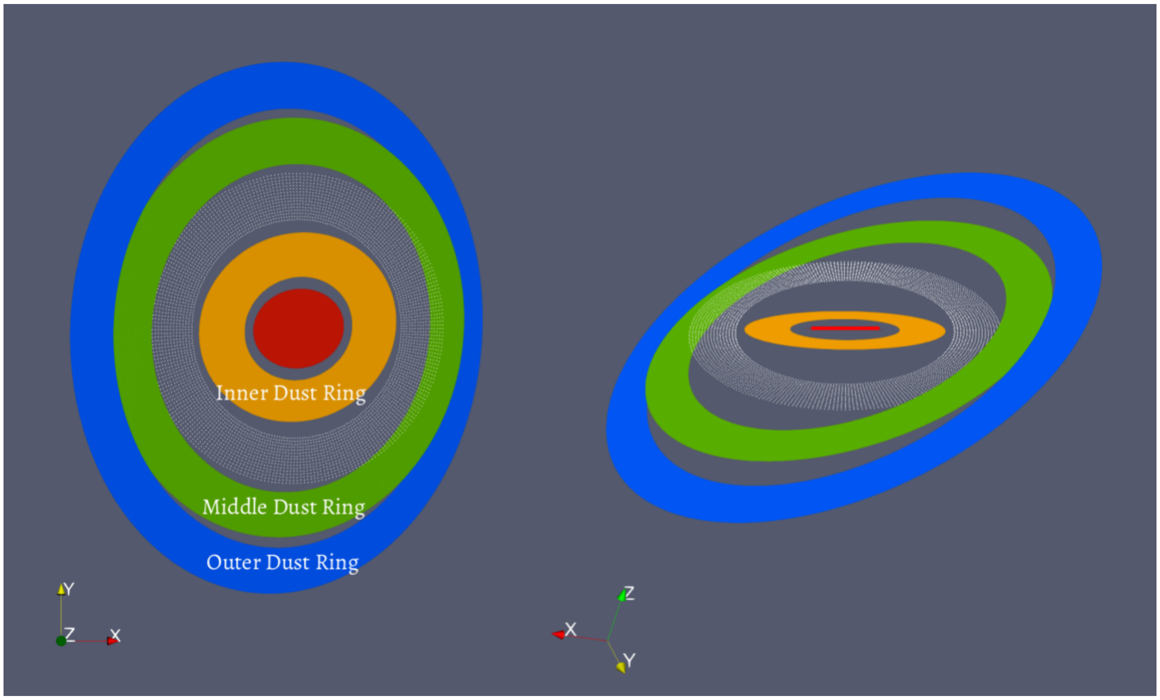

Figure 2.2: A schematic diagram showing the proposed geometry of the GW Ori disk. Orbital planes of the AB-C binary (red), the inner dust ring (orange), the gap between the inner and middle dust rings (white dots), the middle dust ring (green), and the outer dust ring (blue) are marked inside out. The left panel is a sky-projected view, and in the right panel the binary is edge-on. The size of the disk components are not to-scale. The orientation axes are shown at the bottom left corner of each panel, with x-axis being antiparallel to the R.A. direction, y-axis being parallel to the Dec. direction, and z-axis pointing at the observer.

2018). For a protoplanetary disk in the bending-wave regime (i.e., where the aspect ratio is higher than the α-prescription of viscosity; Shakura and Sunyaev 1973), disk parts at different radii shall undergo global precession like a rigid body with possibly a small warp (Smallwood et al. 2019). Therefore the timescale of radial communication of disk materials (i.e., for pressure-induced bending waves propagating at half of the sound speed) and the timescale of global precession determine whether the disk can develop a misalignment inside.

Assuming an inner radius at 32 AU ($3-4$ times the AB-C binary semi-major axis; Czekala et al. 2017; Kraus et al. 2020) and an outer radius at 1300 AU (size of the gas disk, Fang et al. 2017), the global precession time-scale of the entire disk is ~ 0.83 Myr, and the radial communication time-scale is ~ 0.06 Myr (see Appendix A.3.1 and A.3.2 for detailed calculations). The radial communication is able to prevent the disk from breaking or developing a significant warp, and we would not expect the observed large deviations in the inclination and position angle between the inner and middle ring. Therefore, we propose that the gap between the inner and middle ring is deep enough to break the disk into two parts (hereafter the inner and outer disk), undergoing nodal precession independently, due to another mechanism.

Due to the viscous dissipation, the precessing disk is torqued toward either polar alignment (i.e., the binary-disk misalignment becomes 90°; Martin and Lubow 2017; Zanazzi and Lai 2018), or coplanar alignment/counter-alignment. The minimum critical initial binary-disk misalignment for which a disc moves towards polar alignment is $\sim 63°$ in the limit of zero disk mass. Since a higher disk mass will lead to a larger critical angle (Martin and Lubow 2019), the GW Ori disk is most likely moving towards coplanar alignment. As we propose that the disk breaks into two parts undergoing global precession independently, they are also aligning to the binary independently on different time-scales.

Assuming the radial communication is blocked at 60 AU, we estimate the alignment time-scales to be $\sim$ 1 Myr for the inner disk and above 100 Myr for the outer disk (see Appendix A.3.3). This is consistent with the observed significantly smaller inclination of the inner ring with respect to the binary than those of the outer rings. The latter are likely inherited from birth and have not evolved much given the system age.

If the radial communication is also blocked at the gap between the middle and outer ring (e.g., $\sim$ 250 AU), the nodal precession time-scales for the middle and outer ring would be $\sim$ 0.6 Myr and $\sim$ 120 Myr, respectively, and the two rings are likely to develop significantly different position angles. Thus we propose that the gap between the middle and outer ring does not cut off the radial communication, and the two rings precess roughly as a rigid body with only a small warp between them.

2.4.4 Hydrodynamic Simulations

The analytical results suggest that the radial communication is able to prevent the binary from breaking the disk (e.g. Nixon et al. 2013). As a result, we propose a break at $\sim$ 60 AU that is due to other mechanisms in order to explain the observed structures. We carry out a demonstrative smoothed particle hydrodynamic (SPH) simulation with the PHANTOM code (Lodato and Price 2010; Price and Federrath 2010; Price et al. 2018) to test the non-breaking hypothesis in the non-linear regime. The results are shown in Figure 2.3.

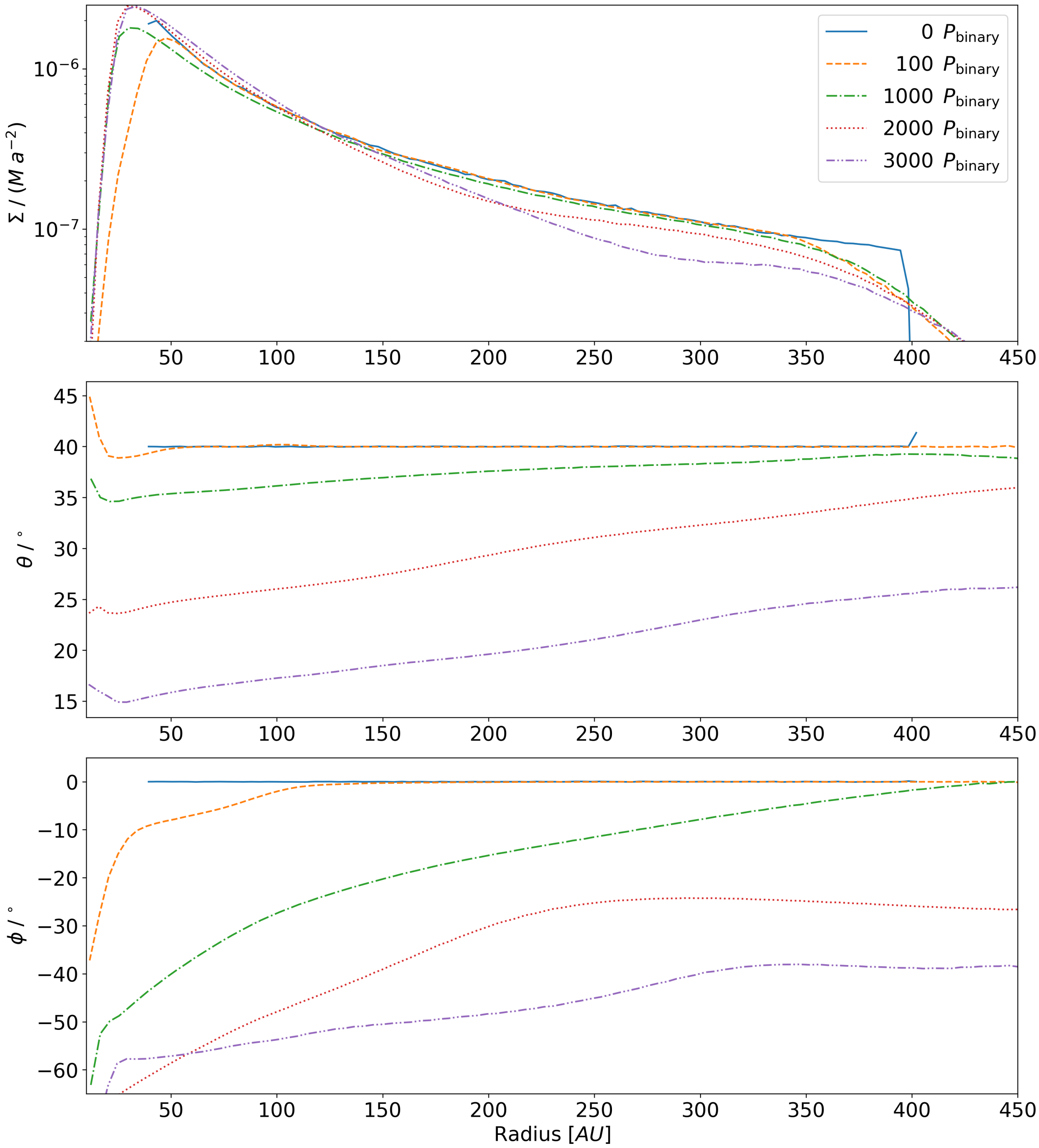

Figure 2.3: The result of the SPH simulation modeling the GW Ori disk. *Upper panel:* Radial profile of the surface density of the disk. M and a are the total mass and separation of the AB-C binary in code units, respectively. *Middle panel:* Radial profile of the binary-disk misalignment. *Lower panel:* Radial profile of the longitude of the ascending node of the disk, measured from the binary's orbital plane.

We model the triple star system as the outer binary in order to speed up the simulation. The simulation consists of 10^6 equal mass Lagrangian SPH particles initially distributed from $r_{\rm in} = 40$ AU to $r_{\rm out} = 400$ AU. The initial truncation radius of the disk does not affect the simulation significantly, since the material moves inwards quickly due to the short local viscous timescale. A smaller initial outer truncation radius $r_{\rm out}$ than what is observed is chosen in order to better resolve the disk. The binary begins at apastron with $e_{\rm b} = 0.22$ and $a_{\rm b} = 9.2$ AU (Czekala et al. 2017). The accretion radius of each binary component is 4 AU. Particles within this radius are accreted, and their mass and angular momentum are added to the star. We ignore the effect of self-gravity since it has no effect on the nodal precession rate of flat circumbinary disks.

The initial surface density profile is taken by

$$\Sigma(r) = \Sigma_0 \left(r/r_0\right)^{-3/2}, \tag{2.7}$$

where Σ_0 is the density normalization at $r_0 = 40$ AU, corresponding to a total disk mass of 0.1 $M_\odot$. We take a locally isothermal disk with a constant aspect ratio $h/r = 0.05$, where h is the scale-height. The Shakura and Sunyaev (1973) α parameter varies in the range $0.008-0.013$ over the disk. The SPH artificial viscosity $\alpha_{\rm AV} = 0.31$ mimics a disk with

$$\alpha \approx \frac{\alpha_{\rm AV}}{10}\frac{\langle H \rangle}{h} \tag{2.8}$$

Lodato and Price (2010), where $\langle H \rangle$ is the mean smoothing length on particles in a cylindrical ring at a given radius and we take $\beta_{\rm AV} = 2$. The disk is resolved with average smoothing length per scale height of 0.32.

The evolution of surface density, binary-disk misalignment, and longitude of the ascending node at different radii suggest that the disk does not show any sign of breaking in 3000 binary's orbital periods (~ 0.04 Myr), which is sufficiently long to tell if the disk would break or not since the radial communication time-scale in the simulation is ~ 0.01 Myr. Instead, the disk presents a global warp. The warp is not taken into account in the analytic estimates. The small outer truncation radius in the simulation leads to a faster precession time-scale than that predicted by the analytic model, comparable to the radial communication time-scale. The simulations suggests that unless the disk is very cool (i.e., low aspect ratio) and in the viscous regime, some other mechanism, e.g., a companion, is needed to break the disk at the gap between the inner and middle ring. This mechanism may also be responsible for producing the observed misalignment in the disk.

A disk with a lower aspect ratio or a higher α value, such that it falls into the viscous regime ($h/r < \alpha$), may break due to the binary's torque (Nixon et al. 2013).

However, observations have suggested lower α values than our adaption here (e.g., $\alpha \lesssim 10^{-3}$, Flaherty et al. 2017). A lower viscosity leads to a larger binary truncation radius (Artymowicz and Lubow 1994), and a longer global precession time-scale (Equation A.4). Therefore we expect even less warping (and no break) in the GW Ori disk than in our simulation.

2.5 Conclusions

We present ALMA 1.3 mm dust continuum observation and ^{12}CO $J = 2-1$ emission of the circumtriple disk around GW Ori. Our main conclusions are the following:

1. For the first time, we identify three dust rings in the GW Ori disk at ~ 46, 188, and 338 AU, with their estimated dust mass being ~ 74, 168, and 245 $M_\oplus$, respectively. The three dust rings have enough solids to make many cores of giant planets ($\sim 10\ M_\oplus$; Pollack et al. 1996).
2. We built three models under various assumptions to fit the dust continuum observations using MCMC fitting. Our results (Table 2.1) suggest that the inner ring has an eccentricity of ~ 0.2, and the three rings have statistically different on-sky projected inclinations. The inner, middle, and outer ring are likely misaligned by ~ 11, 35, and 40 degrees to the orbital plane of the GW Ori AB-C binary system, respectively.
3. A twisted pattern is identified in the first-moment map, suggesting the presence of a warp in the disk, consistent with what we have found in the dust continuum emission.
4. Using analytical analysis and hydrodynamic simulations, we find that the torque from the GW Ori triple stars alone cannot explain the observed large misalignment between the inner and middle dust rings. The disk would not break due to the torque, and a continuous disk is unlikely to show the observed large misalignment. Therefore this hints at some other mechanism that breaks the disk and prevents radial communication of bending waves between the inner and middle ring.

There are still open questions associated with the system. For example, are there any companions in the disk? Dust rings and gaps have been shown to be common in protoplanetary disks (Long et al. 2018; Andrews et al. 2018; Huang et al.

2018; van der Marel et al. 2019), and one of the most exciting hypotheses is that they are produced by embedded companions ranging from stellar-mass all the way to super-Earths (Artymowicz and Lubow 1994; Dong et al. 2015; Zhang et al. 2018). Specifically, a companion may be opening the gap between the inner and middle ring and break the disk there. Companions at hundreds of AU from their host stars have been found before (e.g., HD 106906 b; Bailey et al. 2013). But how they form, i.e., forming in situ or at closer distances, or followed by scattering or migration to the outer regions, is unclear. If GW Ori's dust rings are in the process of forming companions, there will be circumtriple companions, which have not been found before (excluding quadruple systems; Busetti et al. 2018). The system will offer direct clues on the formation of distant companions.

Chapter 3

Planet-induced Meridional Flows of Sub-mm-sized Dust Grains in Protoplanetary Disks

Dust rings associated with planet gaps are often modeled assuming a two-dimensional (2D), razor-thin PPD. Such models either represent a vertically-integrated system, or focus on conditions close to the disk midplane. This is useful, and often necessary, for reducing the computational cost to cover the large parameter space intrinsic to disk-planet interaction (e.g., Zhang and Zhu 2020) and/or to perform high resolution simulations (e.g., Hsieh and Lin 2020; McNally et al. 2019). Indeed, this approximation allows one to construct empirical models of planet gaps based on large sets of simulation data (Kanagawa et al. 2016; Auddy and Lin 2020).

However, real PPDs are three-dimensional (3D). An important effect in 3D is the settling of solids to the disk midplane due to the gravity from the central star in the vertical direction (Dubrulle et al. 1995; Youdin and Lithwick 2007; Laibe et al. 2020). Traditionally, dust settling is assumed to be balanced by turbulent diffusion, resulting in a finite dust layer thickness. This, in turn, directly affects the appearance of dust rings. For example, the sharp, well-defined dust rings observed in the disk around HL Tau suggest that dust grains are well-settled (Pinte et al. 2016).

On the other hand, it is not clear if flattened dust layers are consistent with the interpretation of observed dust rings being produced by giant planets. This is because such planets can induce complex, 3D gas flows (Morbidelli et al. 2014; Szulágyi et al. 2014; Fung and Chiang 2016; Bae et al. 2016; Dong et al. 2019; Teague et al. 2019). Specifically, Fung and Chiang (2016) showed that gap-opening planets induce large-scale meridional circulations around the gap edges, which originate from the differential vertical dependence of planet and viscous torques. If dust grains cannot settle against these meridional circulations, then planet gaps may not explain sharp, well-defined dust rings observed in real PPDs.

In fact, already in a pioneering (pre-ALMA) study, Fouchet et al. (2007) carried out 3D Smoothed Particle Hydrodynamic simulations of planets embedded in dusty disks. Although they did not focus on the issue of meridional flows and dust settling, their simulations indicate that while large meter-sized bodies settle, smaller, cm-sized grains have significantly larger scale-heights. This is an alarming result because grain sizes in the ALMA-observed disks may be even smaller, perhaps only up to 100 μm to 1 mm (Kataoka et al. 2016, 2017; Liu 2019; Zhu et al. 2019), and are thus more easily stirred by gas motions.

The Chapter 3 is organized as follows: We first describe the disk-planet system of interest and its numerical modeling in Section 3.1. We present results in Section 3.2, starting with a fiducial case, followed by a brief parameter survey. Here, we demonstrate that the 'puff-up' of small grains primarily depends on grain size and, to a lesser degree, the planet mass; and is robust against other physical and numerical parameters. We discuss the implications of our results in Section 3.3 and conclude in Section 3.4.

3.1 Disk-planet Model

We consider a 3D protoplanetary disk composed of gas and dust with an embedded planet of mass $M_{\rm p}$ around a central star of mass $M_\star$. We neglect disk self-gravity, magnetic fields, and planet accretion. We use both spherical $\{r, \phi, \theta\}$ and cylindrical $\{R, \phi, Z\}$ coordinates centered on the star. Hereafter we use the subscript '0' to represent evaluations at $(R, Z) = (R_0, 0)$, where R_0 is a reference radius.

The volume density, pressure, and velocity of the gas are denoted by $(\rho_{\rm g}, P, \boldsymbol{V})$. We assume a time-independent, vertically isothermal gas temperature profile

$$T(R) = T_0 \left(\frac{R}{R_0}\right)^{-q}, \tag{3.1}$$

where q is a constant power-law index. The corresponding sound speed is

$$c_{\rm s}(R) = c_{\rm s0} \left(\frac{R}{R_0}\right)^{-q/2}, \tag{3.2}$$

and the gas pressure is

$$P = \rho_{\rm g} c_{\rm s}^2(R). \tag{3.3}$$

The pressure scale-height of gas is defined as

$$H_{\rm g} \equiv \frac{c_{\rm s}}{\Omega_{\rm K}}, \tag{3.4}$$

where $\Omega_{\rm K}(R) = \sqrt{GM_\star/R^3}$ is the Keplerian angular velocity and G is the gravitational constant. Then $h_{\rm g} \equiv H_{\rm g}/R$ is the gas disk aspect ratio. We assume a nonflared gas disk with a constant $h_{\rm g} = 0.05$, corresponding to $q = 1$.

We consider a single species of dust modeled as a pressureless fluid with density and velocity ($\rho_{\rm d}$, $\boldsymbol{W}$). Dust-gas coupling is parameterized by the Stokes number

$$\mathrm{St} \equiv \tau_{\rm s}\Omega_{\rm K}, \tag{3.5}$$

where $\tau_{\rm s}$ is the particle stopping time characterizing the frictional drag force between gas and dust. We consider dust tightly (but imperfectly) coupled to the gas with $\mathrm{St} \ll 1$ (Jacquet et al. 2011).

We assume dust grains are in the Epstein regime with fixed grain size s and internal density $\rho_\bullet$. Then the particle stopping time is $\tau_s = \rho_\bullet s/\rho_{\rm g}c_{\rm s}$ (Weidenschilling 1977). In practice, we adopt the prescription

$$\tau_{\rm s} = \frac{\rho_{\rm g0}c_{\rm s0}}{\rho_{\rm g}c_{\rm s}}\frac{\mathrm{St}_0}{\Omega_{\rm K0}}, \tag{3.6}$$

and choose a reference Stokes number $\mathrm{St}_0 = 10^{-3}$ to represent 100-μm-sized grains with $\rho_\bullet = 1.5$ g cm^{-3} at ~ 45 astronomical units (au) in young PPDs, such as the HL Tau disk[1].

---

[1] Assuming a total disk mass of 0.2 $M_\odot$ (Booth and Ilee 2020), an outer disk radius of 150 au, and a surface density power-law index of -1.5.

3.1.1 Basic equations

The PPD described above is governed by the usual hydrodynamic equations for gas and dust,

$$\frac{\partial \rho_{\rm g}}{\partial t} + \nabla \cdot (\rho_{\rm g} \boldsymbol{V}) = 0, \tag{3.7}$$

$$\frac{\partial \boldsymbol{V}}{\partial t} + \boldsymbol{V} \cdot \nabla \boldsymbol{V} = -\frac{1}{\rho_{\rm g}} \nabla P - \nabla \Phi + \frac{\epsilon}{\tau_{\rm s}} (\boldsymbol{W} - \boldsymbol{V}) + \frac{1}{\rho_{\rm g}} \nabla \cdot \mathcal{T}, \tag{3.8}$$

$$\frac{\partial \rho_{\rm d}}{\partial t} + \nabla \cdot (\rho_{\rm d} \boldsymbol{W}) = 0, \tag{3.9}$$

$$\frac{\partial \boldsymbol{W}}{\partial t} + \boldsymbol{W} \cdot \nabla \boldsymbol{W} = -\nabla \Phi - \frac{1}{\tau_{\rm s}} (\boldsymbol{W} - \boldsymbol{V}). \tag{3.10}$$

$\Phi = \Phi_\star + \Phi_{\rm p} + \Phi_{\rm ind}$ is the net gravitational potential composed of terms from the star, the planet, and the indirect planet-star gravitational interactions. Here $\Phi_\star = -GM_\star/r$, $\Phi_{\rm p}$ and $\Phi_{\rm ind}$ are defined in the section below. $\epsilon \equiv \rho_{\rm d}/\rho_{\rm g}$ is the local dust-to-gas ratio. $\mathcal{T}$ is the viscous stress tensor given by

$$\mathcal{T} = \rho_{\rm g} \nu \left[\nabla \boldsymbol{V} + (\nabla \boldsymbol{V})^\dagger - \frac{2}{3} \boldsymbol{I} \nabla \cdot \boldsymbol{V} \right], \tag{3.11}$$

where ν is the gas kinematic viscosity, and $\boldsymbol{I}$ is the identity tensor.

We include a constant gas kinematic viscosity $\nu = 10^{-5} R_0^2 \Omega_{\rm K0}$, equivalent to $\alpha = 4 \times 10^{-3}$ at R_0 in the conventional α-viscosity prescription (Shakura and Sunyaev 1973). This is to suppress vertical shear instability (VSI; Nelson et al. 2013), which would otherwise stir up dust grains (Flock et al. 2017, 2020; Lin 2019). Similarly, we intentionally omit dust diffusion, which is typically used to represent particle stirring by gas turbulence (e.g., Weber et al. 2019). The chosen viscosity value also suppresses vortex formation (Koller et al. 2003; Li et al. 2005, 2009; Lin and Papaloizou 2010) at the gap edges, which would introduce non-axisymmetry and may also interfere with dust settling (Zhu et al. 2014).

Our disk models are thus designed to minimize known mechanisms that hinder dust settling, so that we can focus on the influence of planet-induced gas flows on axisymmetric dust rings.

3.1.2 Planet

We consider a planet on a fixed, circular orbit at R_0 on the disk midplane. Our fiducial planet mass is $M_{\rm p} = 3 \times 10^{-4} M_\star$, corresponding to a Saturn-mass planet around a solar-mass star. The planet-related potential terms are

$$\Phi_{\rm p} + \Phi_{\rm ind} = -\frac{G m_{\rm p}(t)}{\sqrt{r'^2 + r_{\rm s}^2}} + \frac{G m_{\rm p}(t)}{R_0^2} R \cos{(\phi - \phi_{\rm p})}, \tag{3.12}$$

where $\phi_{\rm p}$ is the azimuth of the planet, $r_{\rm s} = 0.1 H_{\rm g0}$ is a smoothing length,

$$r' = \sqrt{R^2 + R_0^2 - 2 R R_0 \cos{(\phi - \phi_{\rm p})} + Z^2} \tag{3.13}$$

is the distance to the planet, and $m_p(t)$ is a time-dependent planet mass to allow the disk to first reach a quasi-steady state and to avoid transient effects associated with suddenly introducing a massive planet. We insert the planet at a time $t_{\rm i}$ and switch on its potential over a timescale $t_{\rm g}$ by prescribing

$$m_{\rm p}(t) = \begin{cases} 0 & t \leq t_{\rm i}, \\ \frac{1}{2}\left[1 - \cos\left(\frac{t - t_{\rm i}}{t_{\rm g}} \pi\right)\right] M_{\rm p} & t_{\rm i} < t \leq t_{\rm i} + t_{\rm g}, \\ M_{\rm p} & t > t_{\rm i} + t_{\rm g}. \end{cases} \tag{3.14}$$

Unless otherwise stated, we adopt $t_{\rm i} = 2000 P_0$ and $t_{\rm g} = 500 P_0$, where $P_0 = 2\pi\Omega_{\rm K0}^{-1}$ is the planet's orbital period. The planet masses we consider are expected to open dust gaps (Rosotti et al. 2016).

3.1.3 Gas and Dust Initialization

The gas density is initialized to

$$\rho_{\rm g} = \rho_{\rm g0} \left(\frac{R}{R_0}\right)^{-p} \times \exp\left[\frac{G M_\star}{c_{\rm s}^2}\left(\frac{1}{r} - \frac{1}{R}\right)\right], \tag{3.15}$$

with $p = 1.5$. The reference gas density $\rho_{\rm g0}$ is arbitrary for a non-self-gravitating disk. For a thin disk ($|z/R| \ll 1$) the vertical gas profile is Gaussian ($\propto \exp{[-z^2/2H_{\rm g}]}$). The dust is initialized to $\rho_{\rm d} = \epsilon \rho_{\rm g}$ with a uniform local dust-to-gas ratio $\epsilon = 0.05$, except towards the radial boundaries where it is tapered to zero.

We follow Kanagawa et al. (2017) and initialize the gas and dust azimuthal velocities to

$$V_\phi = R\,\Omega_\mathrm{K}(R)\left(\sqrt{1-2\eta}+\frac{\epsilon\eta}{\epsilon+1}\frac{1}{\mathrm{St}'^2+1}\right) \tag{3.16}$$

$$W_\phi = r\,\Omega_\mathrm{K}(r) - R\,\Omega_\mathrm{K}(R)\left(\frac{\eta}{\epsilon+1}\frac{1}{\mathrm{St}'^2+1}\right), \tag{3.17}$$

where

$$\eta = \frac{1}{2}\left[(p+q)h_\mathrm{g}^2 + q\left(1-\frac{R}{r}\right)\right] \tag{3.18}$$

is a dimensionless measure of the global radial pressure gradient and and $\mathrm{St}' = \mathrm{St}/(1+\epsilon)$. The radial velocities are initialized to

$$V_\mathrm{R} = \frac{2\epsilon\eta}{\epsilon+1}\frac{\mathrm{St}'}{\mathrm{St}'^2+1}R\,\Omega_\mathrm{K}(R) \tag{3.19}$$

$$W_\mathrm{R} = -\frac{2\eta}{\epsilon+1}\frac{\mathrm{St}'}{\mathrm{St}'^2+1}R\,\Omega_\mathrm{K}(R). \tag{3.20}$$

These correspond to the inward drift of dust due to the radial pressure gradient and a compensating outward drift of gas due to angular momentum conservation. The vertical velocities $V_\mathrm{Z}, W_\mathrm{Z}$ are set to zero initially.

Note that we neglect the viscous accretion (Lynden-Bell and Pringle 1974) in the initial gas velocity field. In a 2D disk, this viscous radial gas flow is given by

$$V_\mathrm{vis}^\mathrm{2D} = -\frac{3\nu}{R}\frac{d\ln\left(\nu\Sigma_\mathrm{g}R^{1/2}\right)}{d\ln R}, \tag{3.21}$$

where $\Sigma_\mathrm{g} = \int_{-\infty}^{\infty}\rho_\mathrm{g}dz$ is the gas surface density. For our chosen mid-plane gas density profile (Equation 3.15) we have $\Sigma_\mathrm{g} \propto R^{-1/2}$. Then for a constant ν, as considered throughout this work, $V_\mathrm{vis}^\mathrm{2D} = 0$. Thus our disk models have, in an averaged sense, no net viscous accretion.

In any case, the precise initial conditions are unimportant because we allow the disk to first relax to a quasi-steady state before inserting the planet.

3.1.4 Numerical method

We evolve the above dusty disk using the FARGO3D code (Benítez-Llambay and Masset 2016). FARGO3D is a general-purpose finite-difference code, and is particularly suited for simulating protoplanetary disks as it includes the FARGO algorithm (Masset 2000) that alleviates time-step constraints imposed by the fast rotation at the inner disk boundary.

We adopt a spherical domain centered on the star with $r \in [0.4, 2.0]R_0$, $\phi \in [0, 2\pi]$, and polar angle such that $\tan(\frac{1}{2}\pi - \theta) \in [0, 3]h_{\mathrm{g}}$, i.e. three gas scale-heights above the midplane. Note that we only consider the half-disk with $Z \geq 0$ to further reduce computation time. The resolutions we choose are $N_r \times N_\theta \times N_\phi = 250 \times 60 \times 720$, with logarithmic spacing in r and uniform spacing in θ and ϕ. We thus resolve H_{g} by approximately 20 cells vertically, 8 cells radially, and 6 cells azimuthally. The simulations are run in the co-rotating frame with the planet.

At the radial boundaries, the gas density is fixed to its initial value, while the dust density is symmetric. At the disk surface we assume the gas is in vertical hydrostatic equilibrium. We set the dust and gas meridional velocities to zero at the radial and upper disk boundaries, and azimuthal velocities are taken to be Keplerian with a pressure offset for the gas. Reflective boundaries are imposed at the disk midplane. Periodic boundaries are imposed in ϕ direction. We do not apply damping zones (cf., De Val-Borro et al. 2006). The total mass of gas and dust is conserved with these boundary conditions.

3.1.5 Diagnostics

To analyze our results, we first convert simulation outputs from spherical to cylindrical coordinates using cubic interpolation. Motivated by observations of rings and gaps, we mostly examine azimuthally averaged profiles, which is representative since non-axisymmetric features are weak and only appear close to the planet. Nevertheless, we mask the planet by only considering values in the region $\phi - \phi_{\mathrm{p}} \in [\psi, 2\pi - \psi]$ when calculating azimuthal averages, where $\psi = \arcsin(3R_{\mathrm{H}}/R_0)$ denotes the angular distance of three Hill radii, which is defined as $R_{\mathrm{H}} = R_0\sqrt[3]{M_{\mathrm{p}}/(3M_\star)}$.

We are primarily interested in the thickness of the dust layer. We define and obtain the dust scale-height $H_{\mathrm{d}}(R)$ by fitting

$$\rho_{\mathrm{d}}(R, Z) = \rho_{\mathrm{d}}(R, 0) \times \exp\left(-\frac{Z^2}{2H_{\mathrm{d}}^2}\right). \tag{3.22}$$

However, for well-settled dust we find the dust profile cannot be accurately fitted by a Gaussian[2]. In such cases we obtain the dust scale-height by searching where

$$\rho_{\rm d}(R, 2H_{\rm d}) = \rho_{\rm d}(R, 0) \times \exp(-2) \tag{3.23}$$

is satisfied. This definition of the dust layer thickness is more robust, and coincides with Equation 3.22 when the distribution is close to Gaussian.

3.2 Results

In this section, we first compare our fiducial result with previous 2D studies. Secondly, we describe the dust kinematics in our fiducial simulation. Thirdly, we discuss the origin of dust behavior. Finally, we briefly explore the effect of disk parameters.

3.2.1 Disk Morphology in the Ecliptic Plane

Figure 3.1 shows the gas and dust surface density distributions at $5000P_0$, which were obtained by integrating the volume densities through the disk column. The planet opens a gap of 5–6 $R_{\rm H}$ wide in the gas disk, which is consistent with the empirical result in Kanagawa et al. (2016) based on 2D simulations. Dust is more cleared compared with gas, but there are still some remaining in the horseshoe orbits. We note the axisymmetric, dust rings at the outer gap edge, indicative of dust trapping. Other than the planet-induced spiral arms within $\sim 3R_{\rm H}$ of the planet, non-axisymmetric features are weak in the disk.

While the dust is migrating inwards due to the radial pressure gradient, the gas gains angular momentum from dust back-reaction and migrates outwards. Besides, the gas in the outer disk gains angular momentum from the interactions with the planet. These two mechanisms lead to the gas surface density decreasing in the inner part of the disk and increasing in the outer part.

Although our models are 3D, these surface density maps are qualitatively similar to early 2D simulations (Paardekooper and Mellema 2006). More importantly, the dust gap of sub-mm-sized grains induced by our Saturn-mass planet, which is equivalent to $100M_\oplus$ or $0.3M_{\rm J}$, is expected to be observable by ALMA (Rosotti et al. 2016).

The similarity between 2D and 3D simulations in the gas surface densities has

---

[2] The least-squares fitting function returns the input parameters of initial guess instead of solutions corresponding to a local minimum of the cost function.

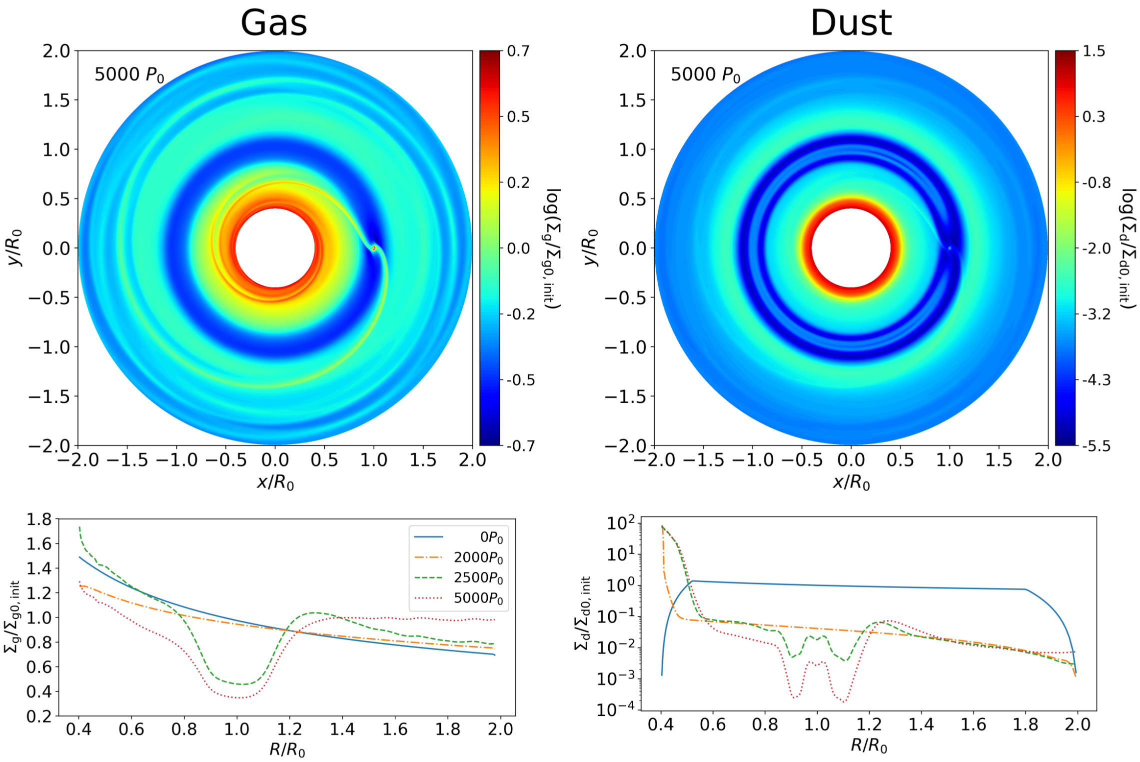

Figure 3.1: Distributions gas (left) and dust (right) surface densities. The snapshots are taken from the fiducial simulation with a Saturn-mass planet and dust grains with $\mathrm{St}_0 = 10^{-3}$. *Upper panels*: Ecliptic plots at the end of the the simulation ($5000P_0$). *Lower panels*: Azimuthally averaged (excluding azimuth within $\arcsin(3R_\mathrm{H}/R_0)$ to the planet) radial profiles at 0, 2000, 2500, and $5000P_0$. All panels are normalized to the initial value at R_0.

already been pointed out by Fung and Chiang (2016), which indicates that 2D simulations are sufficient to obtain a representative gas morphology. On the other hand, we find below that the vertical distribution of dust can be significantly affected by the planet, which requires 3D modeling.

3.2.2 Dust Lofted above the Disk Midplane

Figure 3.2 shows the meridional snapshots of the local dust-to-gas ratio at ages 0, 2000, 2500, and $5000P_0$, respectively. Figure 3.3 shows the time evolution of the normalized dust scale-height $H_\mathrm{d}/H_\mathrm{g}$, and the particle stopping time at different disk heights at $5000P_0$.

We recognize that dust grains first settle to a thin layer due to stellar gravity. The timescale of settling is on the order of $10^3\,\Omega_\mathrm{K0}^{-1}$, which is consistent with the results in

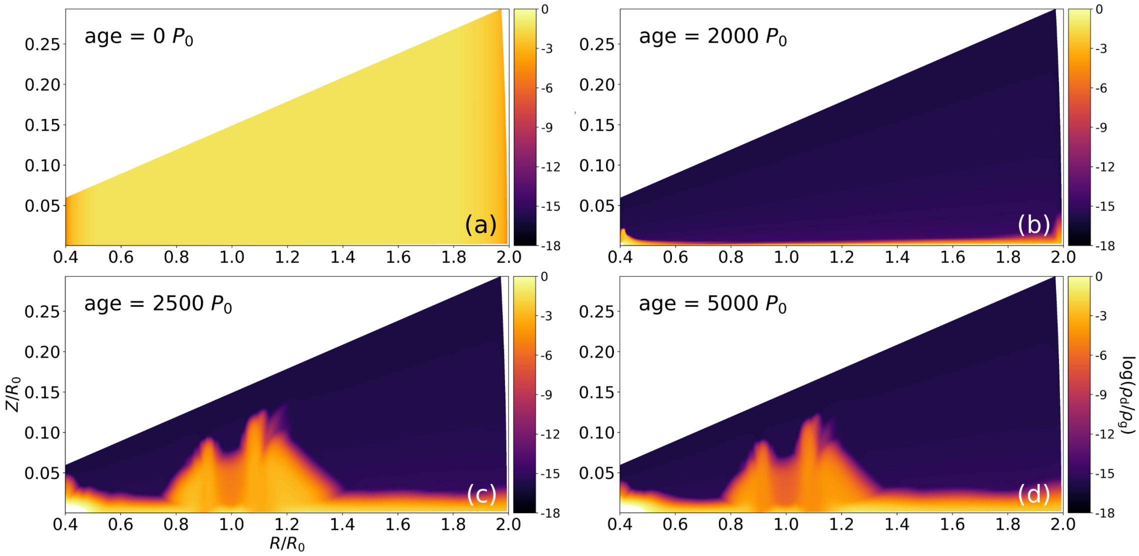

Figure 3.2: Meridional distributions of the dust-to-gas ratio. The values are azimuthally averaged (excluding azimuth within $\arcsin(3R_{\rm H}/R_0)$ to the planet) and taken at 0, 2000, 2500, and $5000P_0$ from the fiducial simulation (with a Saturn-mass planet and dust grains with $\mathrm{St}_0 = 10^{-3}$). Colors are mapped in the logarithmic scale.

Nakagawa et al. (1981) and Takeuchi and Lin (2002). The timescale of radial drift is comparable to that of settling, leading to a considerable amount of dust having migrated to the inner disk during settling.

Once the planet is inserted (at $2000P_0$) and its mass starts to increase, we find dust is efficiently lofted above the disk midplane up to 2–3 $H_{\rm g}$ at the gap edges, with a characteristic dust scale-height $\sim 0.8H_{\rm g}$.

3.2.3 Origin of the 'Puff-up'

Figure 3.4 shows the streamlines of dust and gas plotted over the local dust-to-gas ratio at the end of the fiducial simulation. The flow pattern of gas qualitatively agrees with the results in Fung and Chiang (2016). It also shows that in the 'puff-up' regions ($R \sim 0.9R_0$ and $1.1R_0$, $Z \leq 2H_{\rm g0}$), the dust and gas velocity streamlines are similar, indicating that the dust kinematics there is closely related to the gas kinematics.

This result is expected for the small grains we consider. In this limit, the gas and dust kinematics can be related by the terminal velocity approximation (Youdin and Goodman 2005; Jacquet et al. 2011; Price and Laibe 2015; Lovascio and Paardekooper

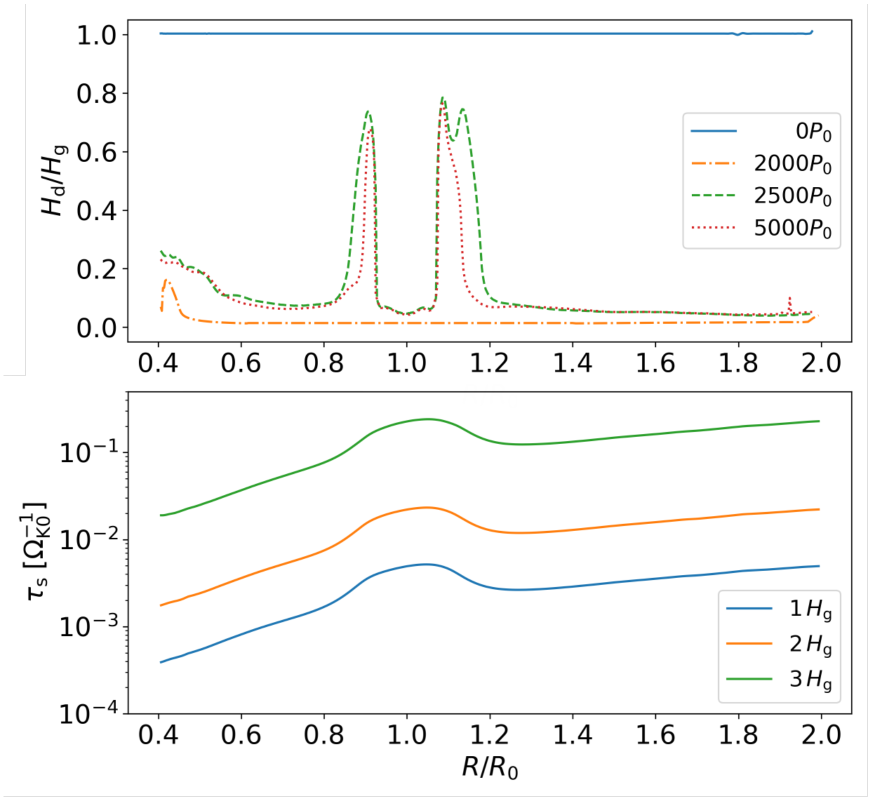

Figure 3.3: Radial Profiles of the dust scale-height and the particle stopping time. *Upper:* Radial profiles of the normalized dust scale-height at 0, 2000, 2500, and $5000P_0$. *Lower:* Radial profiles of the particle stopping time at $Z = 1$, 2, and 3 H_g at $5000P_0$. Both panels are azimuthally averaged (excluding azimuth within $\arcsin(3R_H/R_0)$ to the planet) and taken from the fiducial simulation with a Saturn-mass planet and dust grains with $\mathrm{St}_0 = 10^{-3}$.

2019):

$$\boldsymbol{W} = \boldsymbol{V} + \frac{\nabla P}{\rho}\tau_s, \tag{3.24}$$

where $\rho \equiv \rho_g + \rho_d$ is the total density.

This approximation (validated in Appendix B.1) shows that, for tightly coupled grains, its velocity is almost equal to the gas velocity, with a correction due to local pressure gradients. In PPDs, the vertical pressure gradient approximately balances the vertical gravity from the star, which causes dust to settle (Dubrulle et al. 1995; Takeuchi and Lin 2002). Thus, for dust to be lofted upwards, the gas vertical velocity must be upward and overwhelm the downward stellar gravity.

Figure 3.5 shows the absolute ratio between the two terms on the right-hand-side of Equation 3.24. A smaller ratio indicates a larger contribution to the dust

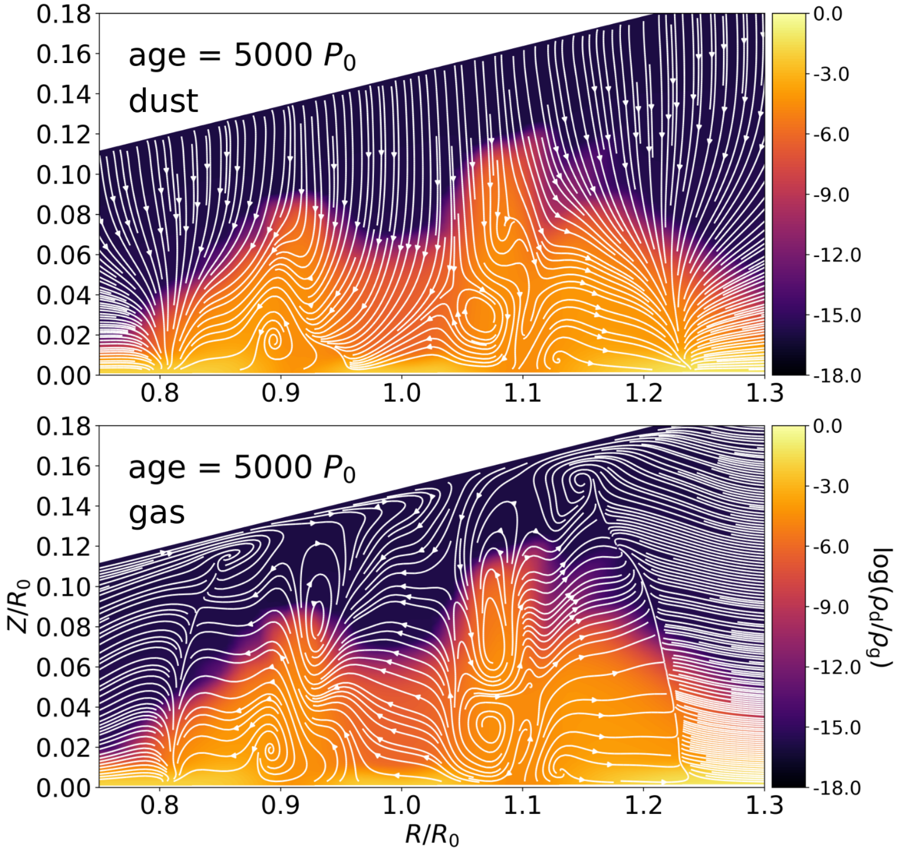

Figure 3.4: Streamlines of dust and gas flows. The snapshots are taken at the end of the fiducial simulation (with a Saturn-mass planet and dust grains with $\mathrm{St}_0 = 10^{-3}$). Both panels are azimuthally averaged (excluding azimuth within $\arcsin(3R_\mathrm{H}/R_0)$ to the planet) and plotted over the dust-to-gas ratio (part of Figure 3.2d). Both the vertical flows towards the planet and the flows repelled from the planet are masked out. The gap-crossing flux indicates that the gap is not deep enough to prohibit material transport.

velocities from the gas flow. We find that inside the gap, the vertical dust velocities are dominated by the pressure gradient throughout vertical extent. Outside the gap, the same is true at high altitudes ($Z \gtrsim H_{\mathrm{g}0}$), leading to settling, while it is the other way around close to the midplane.

Figure 3.5 also shows the Mach number in the vertical direction $\mathrm{Ma} \equiv V_\mathrm{z}/c_\mathrm{s}$. At the 'puff-up' radii ($\sim$ 0.9 and 1.1 R_0), the upward velocity of gas reaches $0.01c_\mathrm{s}$, roughly consistent with Fung and Chiang (2016). Given the dust settling speed $W_\mathrm{sed} \sim \mathcal{O}(c_\mathrm{s}\mathrm{St})$ (Takeuchi and Lin 2002), we can expect the settling of grains to be disrupted by gas meridional flows when $|\mathrm{Ma}| \gtrsim \mathrm{St}$, which is easily satisfied in our fiducial case with $\mathrm{St} \sim 10^{-3}$.

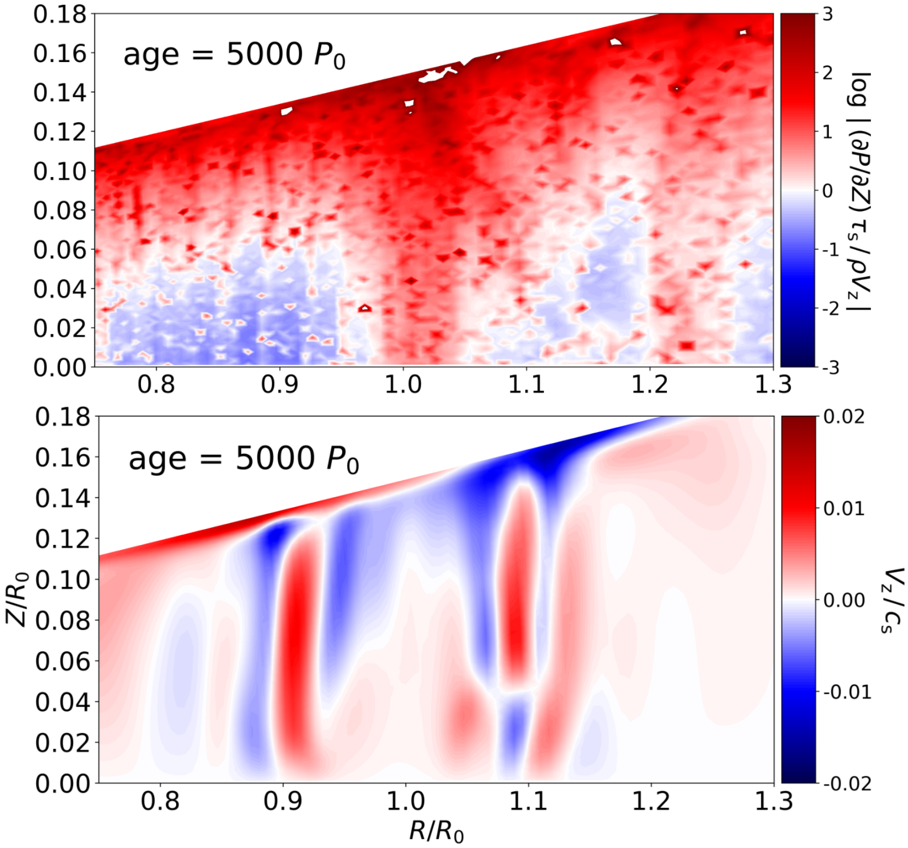

Figure 3.5: Meridional distributions of the terminal velocity approximation and the vertical Mach number. *Upper*: The absolute ratio between the two terms on the right hand side of the terminal velocity approximation (Equation 3.24) in the vertical direction. Red (blue) indicates dust velocities are dominated by the local pressure gradient (gas flow). *Lower*: Vertical Mach number of gas. Red (blue) denotes upward (downward) velocities. Both panels are azimuthally averaged (excluding azimuth within $\arcsin(3R_{\rm H}/R_0)$ to the planet) and taken at the end of the fiducial simulation (with a Saturn-mass planet and dust grains with $\mathrm{St}_0 = 10^{-3}$).

The mechanism of planet-induced meridional gas flows has been analyzed in detail by Fung and Chiang (2016). The planet's Lindblad torques drive gap-opening gas flows away from the planet, which encounter gap-closing gas flows toward the planet driven by viscous torques. The magnitude of these opposing torques depend on height, and the net effect is the meridional circulation: an upward combined flow near the gap edges and a downward flow close to the planet's orbit. Our simulations show that dust particles are then swept up by these circulations.

Therefore, we conclude that the 'puff-up' of dust on the gap edges is due to

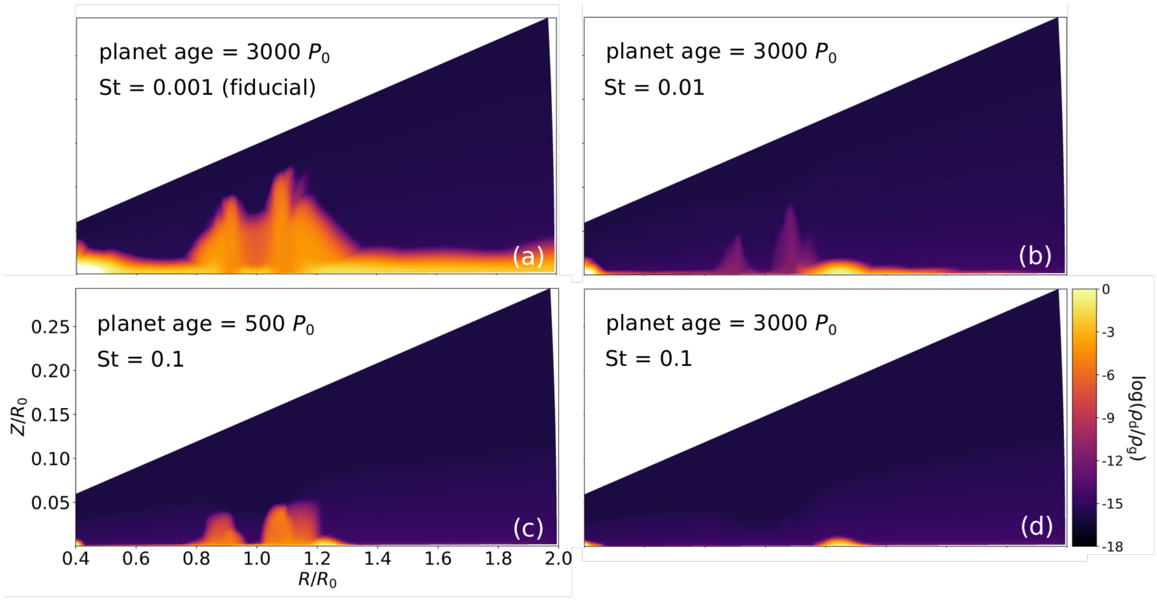

Figure 3.6: Meridional distributions of the dust-to-gas ratio from the parameter study (1). The values are azimuthally averaged (excluding azimuth within $\arcsin(3R_\mathrm{H}/R_0)$ to the planet). (a): From the fiducial run ($\mathrm{St}_0 = 0.001$). (b): From the $\mathrm{St}_0 = 0.01$ run. (c)–(d): From the $\mathrm{St}_0 = 0.1$ run. Panel (a), (b) and (d) are taken at $3000P_0$ after the planet is introduced in the simulations.

planet-induced meridional gas flows.

3.2.4 Parameter study

We now carry out a brief parameter study to examine the effect of disk-planet properties on the dust 'puff-up' observed in the fiducial case above. Specifically, since the dust is lofted by meridional gas flows induced by the planet, we expect that larger grains would lessen this effect. On the other hand, larger planet masses should lead to larger 'puff-ups'. Figure 3.6 and 3.7 show the dust-to-gas ratios in these simulations. We also check that the metallicity (or dust loading) and numerical parameters have insignificant effects.

Effect of Stokes Number

A larger grain size or Stokes number leads to weaker coupling between gas and dust. That is, the magnitude of the second term in the terminal velocity approximation increases with St_0 (Equation 3.24), which favors dust settling. As discussed above, for

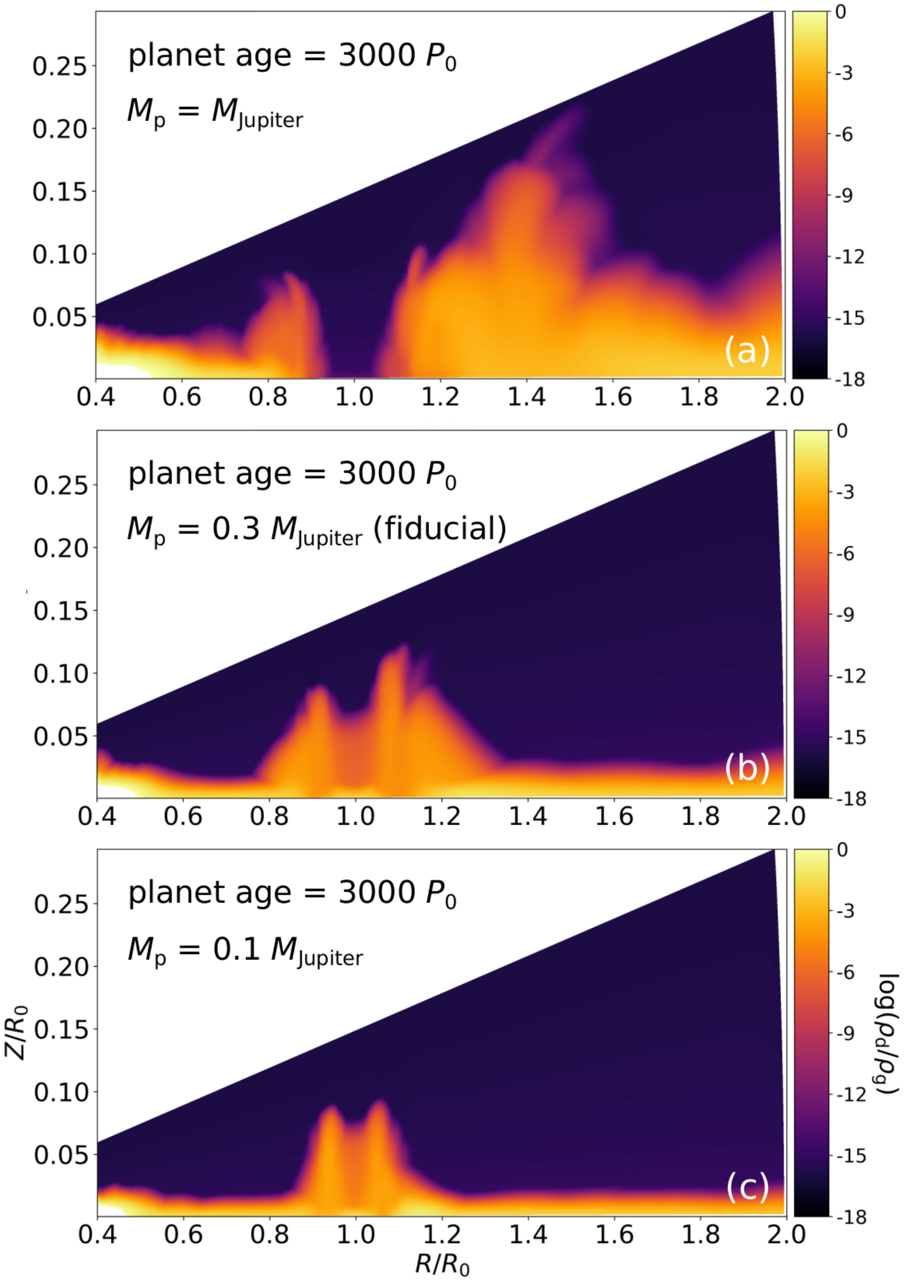

Figure 3.7: Meridional distributions of the dust-to-gas ratio from the parameter study (2). The values are azimuthally averaged (excluding azimuth within $\arcsin(3R_{\rm H}/R_0)$ to the planet) dust-to-gas ratio at the end of each simulation. (a): From the Jupiter-mass planet run. (b): From the fiducial run (Saturn-mass/0.3 Jupiter-mass planet). (c): From the 0.1 Jupiter-mass planet run. All panels are taken at $3000P_0$ after the planet is introduced in the simulations (i.e., disk age of $5000P_0$).

Saturn-mass planets that induce vertical flows with $|\mathrm{Ma}| \sim 0.01$, we expect particles with $\mathrm{St} \gtrsim 0.01$ to be much more resilient to being puffed up.

We thus consider two simulations with $\mathrm{St}_0 = 0.01$ and $\mathrm{St}_0 = 0.1$, respectively. We insert the planet at $500P_0$ in the $\mathrm{St}_0 = 0.01$ case and at the beginning ($t_\mathrm{i} = 0$) in the $\mathrm{St}_0 = 0.1$ case, since these larger grains have much shorter settling timescales ($< 500P_0$) compared with the fiducial case. These simulations are shown in Figure 3.6b–d, which can be compared to the fiducial run in Figure 3.6a.

We find that after $3000P_0$ since the planet is introduced in the $\mathrm{St} = 0.01$ case (Figure 3.6b), the 'puff-up' is much weaker than the fiducial run, with $H_\mathrm{d}/H_\mathrm{g} \lesssim 0.3$ (cf., 0.8 in the fiducial case). Due to the larger Stokes number, particles also drift inwards more rapidly (Equation 3.24) and pile up at the inner disk due to the closed boundary conditions. We find a wide ($\sim 8H_{\mathrm{g}0}$) dust ring forming exterior to the planet ($R \gtrsim 1.2R_0$) due to a local pressure maximum, but it remains flat with $H_\mathrm{d}/H_\mathrm{g} \lesssim 0.05$, since planet-induced vertical flows of gas mostly lie closer in.

For $\mathrm{St}_0 = 0.1$, we find that planet-disk interactions can still trigger the dust 'puff-up' (Figure 3.6c), but this effect is transient as it disappears by $3000P_0$ after the planet is introduced (Figure 3.6d). In this case, dust is rapidly lost through radial drift, leaving only dust trapped at the local pressure maximum exterior to the planet. The end result is a single, narrow, and well-settled dust ring with width $\sim 2H_\mathrm{g}$ and thickness $H_\mathrm{d}/H_\mathrm{g} \lesssim 0.05$ at $R \sim 1.2R_0$.

Effect of Planet Mass

We here repeat the fiducial run with a Jupiter-mass planet ($M_p = 10^{-3}M_\star$). A more massive planet is expected not only to create a deeper and wider gap (Kanagawa et al. 2016), but also to drive stronger meridional gas flows around the gap edges (Fung and Chiang 2016).

Figure 3.7a shows the distribution of the local dust-to-gas ratio at the end of the simulation. We find that a higher planet mass leads to stronger and more complicated meridional gas flows around the outer gap edge, with radial extent $\gtrsim 8H_{\mathrm{g}0}$ and $|\mathrm{Ma}| \sim 0.04$. Those for the gas flows at the inner gap edge remain similar to the fiducial case, with radial extent $\lesssim 2H_{\mathrm{g}0}$ and $|\mathrm{Ma}| \lesssim 0.02$. As a result, we find a more significant dust 'puff-up' at the outer gap edge, especially in its radial extent, $1.2R_0 \lesssim R \lesssim 1.6R_0$. Dust beyond the outer gap edge is also puffed-up more significantly than the fiducial case, with $H_\mathrm{d}/H_\mathrm{g} \gtrsim 0.15$. However, we notice that the 'puff-up' at the inner gap edge is actually weaker than the fiducial case, with only $H_{\rm d}/H_{\rm g} \lesssim 0.4$. We attribute this effect to a larger particle stopping time at the inner gap edge due to stronger gap-opening effect by the Jupiter-mass planet. This produces a lower gas density, lessens the dust-gas coupling (since $\tau_{\rm s} \propto \rho_{\rm g}^{-1}$, see Equation 3.6) and leads to more efficient dust settling.

To test if sub-mm-sized grains can settle against a less massive, but still gap-opening planet, we also present a simulation with $M_{\rm p} = 10^{-4}M_\star$, which corresponds to $0.1M_{\rm J}$ or $30M_\oplus$. For comparison, Rosotti et al. (2016) find $M_{\rm p} \gtrsim 20M_\oplus$ is needed to induce dust rings (see also Lambrechts et al. 2014). The result is shown in Figure 3.7c, where we find that the dust 'puff-up' still exists, with $H_{\rm d}/H_{\rm g}$ at the inner and outer gap edges being ~ 0.6 and 0.5, respectively.

Additional simulations

We ran additional simulations to confirm that the dust 'puff-up' by planet-disk interaction is a robust phenomenon.

Metallicity Our simulations include full back-reaction from dust onto gas. In this case, the global dust-to-gas ratio, or metallicity, can be important when considering vertical flows. This is because metallicity introduces a stabilizing effective buoyancy force (Lin and Youdin 2017), which can favor dust settling (Lin 2019).

In our standard approach of allowing dust to first settle, considerable radial drift of dust also occurs. Thus when the planet is introduced, the midplane dust-to-gas ratio around the planet is only $\mathcal{O}(10^{-2})$, so that dust feedback does not take effect. This was confirmed with an additional run initialized to $\epsilon = 0.1$. Thus to evaluate the importance of dust feedback, we simulated a disk where ϵ is initialized to $\epsilon_0 \exp\left(-Z^2/2H_\epsilon^2\right)$, with $H_\epsilon^{-2} \equiv H_{\rm d}^{-2} - H_{\rm g}^{-2}$ and $H_{\rm d} = 0.1H_{\rm g}$. We set $\epsilon_0 = 1$ (so the overall metallicity is ~ 0.1) and insert the planet at $t_i = 0$ so that it immediately interacts with a dust-rich environment. However, we found that the dust 'puff-up' in this case, where dust back-reaction is expected to be non-negligible, was in fact quite similar to that in the fiducial case. Thus the dust back-reaction is unimportant to the 'puff-up'. This is likely due to the small Stokes numbers considered herein, so that the dust-gas system behaves close to a single fluid and both are stirred up by the planet.

Radial Domain Extent We examine whether the radial domain extent could affect the dust 'puff-up' at the outer gap edge ($R \sim 1.1R_0$) by rerunning the fiducial case with an extended radial domain of 0.4 – 4.0 R_0, but with the same amount of radial grid cells. Thus we resolve H_g with ~ 5.5 cells. We again find that the 'puff-up' pattern show no differences from the fiducial case. However, a more prominent dust ring forms at the local pressure maximum exterior to the planet, due to the fact that more dust is contained in the domain, which have migrated from the outer disk.

This experiment shows that the dust 'puff-up' is a radially localized phenomenon and is thus insensitive to boundary conditions. We expect the same result at the inner gap edge with a reduced inner boundary, but this is difficult to test explicitly as it adds substantial computation cost.

Resolution We also rerun the fiducial simulation with a doubled vertical resolution (i.e., 40 cells per $H_{\mathrm{g}0}$) to examine whether resolution could affect the dust 'puff-up'. We found that the 'puff-up' in this high-resolution run was identical to the fiducial case. This confirms the origin of the 'puff-up' from vertically-global gas meridional flows, which can be resolved with the fiducial resolution (see also Fung and Chiang 2016).

3.3 Discussion

Here we briefly discuss a few inspirations that the planet-induced dust 'puff-up' effect has brought, and introduce a few aspects that can be fulfilled in the future studies.

3.3.1 Dust settling against planet-stirring

The finite thickness of dust layers is usually attributed to particle stirring by gas turbulence (Fromang and Papaloizou 2006; Zhu et al. 2015; Flock et al. 2017, 2020), which can be modeled as a diffusion process with the particle scale-height given by

$$H_\mathrm{d} = \sqrt{\frac{\delta}{\mathrm{St} + \delta}} H_\mathrm{g} \tag{3.25}$$

(Dubrulle et al. 1995; Youdin and Lithwick 2007), where δ is a dimensionless measurement of particle diffusion by gas turbulence. Our simulations are laminar, and particles are stirred by planet-induced, vertically-global meridional flows (Fung and Chiang 2016) instead of turbulence. Nevertheless, we could apply Equation 3.25 to our fiducial simulation to obtain an effective δ, which was found to be $\sim \mathcal{O}(10^{-3})$ at the gap edges, to place our results in the wider context of dust settling in protoplanetary disks.

3.3.2 Inspirations to Observations

Recent disk surveys have shown that dust gaps and rings are common in PPDs (Andrews et al. 2018; Huang et al. 2018; Long et al. 2018; van der Marel et al. 2019). The origin of these rings are still being debated, although disk-planet interaction is frequently invoked (Dipierro et al. 2015; Jin et al. 2016; Toci et al. 2020; Pinte et al. 2020). Here, a common approach is to first perform 2D disk-planet simulations, then construct a 3D dust distribution assuming a turbulent diffusion model (e.g., Equation 3.25; Dubrulle et al. 1995), before producing a synthetic image via radiative transfer and comparing it with observations (e.g., Dong et al. 2015; Jin et al. 2016; Facchini et al. 2020).

However, our simulations show that while gap-opening planets naturally produce dust rings, they also easily stir up sub-mm-sized grains to high elevations. The meridional dust distribution is non-trivial. It must therefore either be obtained from explicit 3D disk-planet simulations, or otherwise accounted for using knowledge synthesized from 3D simulations. Dust structures with realistic vertical extent should be used as input for radiative transfer calculations to produce synthetic images, especially when the sharpness of the rings and gaps are concerned.

Observations, on the other hand, indicate that at least some observed dust rings are well-settled due to their sharp appearance (Pinte et al. 2016). We thus suggest that the observed or inferred dust layer thickness may be used to distinguish dust rings formed by gas-gap-opening planets from those formed by other mechanisms that do not simultaneously stir up dust (e.g., snowlines, Zhang et al. 2015). That is, the former should produce thicker dust rings. Conversely, within the planet interpretation, the sharpness of dust rings can be used to place an lower limit on the grain size.

For example, Jin et al. (2016) find that three planets of around Saturn mass can account for the three well-defined dust gaps observed around HL Tau, assuming mm-sized grains. In their disk models such grains have Stokes numbers around 10^{-3} to 10^{-2} around the gaps. These parameter values are comparable to our fiducial case. We thus expect dust rings (or gap edges) to be puffed-up, making the gaps and rings less prominent. This suggests grains should in fact be larger than mm-sized.

A more direct measurement of dust 'puff-up' is the inclination of dust rings. Here, we highlight the recent result from Huang et al. (2020), who reported that a dust ring at ~ 84 au in the disk around GM Aur is found to have different shapes between its inner and outer edge. One of the possible explanations to the observation is that the ring has a finite thickness. Considering dust grains of 100 μm size at that location, we find a Stokes number of $\sim 5 \times 10^{-3}$, assuming a total disk mass of 0.18 $M_{\odot}$, an outer disk radius of 450 au, a surface density power-law index of -1.5, and a grain density of 1.5 g cm^{-3} (McClure et al. 2016; Huang et al. 2020). Our simulations then suggest that the observed ring morphology might result from the dust 'puff-up' by a young, Saturnian planet in the disk, which is within the planet mass range estimated by Huang et al. to carve the dust gap just interior to the dust ring.

Finally, although planets are one of the most popular explanations for rings and gaps, only a few planets have been directly detected in PPDs (e.g., PDS 70b/c; Keppler et al. 2018; Haffert et al. 2019). Given that many of the disks are not face-on, we suggest that there could be planets obscured by the walls of the dust 'puff-up', causing extinction of planets in observations of near infrared and optical wavelengths.

3.3.3 Caveats and outlooks

The cost of full 3D simulations only allowed us to conduct a brief parameter study to qualitatively show that the dust 'puff-up' by gap-opening planets is a robust phenomenon. A larger number of simulations is needed in more comprehensive studies to work out an empirical formula for the dust 'puff-up' as a function of grain size and the planet mass. For example, one can fit dust scale-heights according to Equation 3.25 and quantify the effective particle diffusion caused by planet-stirring as a function of planet mass and dust size.

We have considered planet masses larger than the thermal mass $M_{\rm th} = h_{\rm g}^3 M_{\star}$ ($\sim 10^{-4} M_{\star}$), for which planets are expected to open gas gaps (Korycansky and Papaloizou 1996; Goodman and Rafikov 2001). However, lower planet masses can open gaps in dust with little perturbation to the gas (Rosotti et al. 2016; Dipierro and Laibe 2017; Dong et al. 2017; Chen and Lin 2018). Such planets may not induce strong 3D meridional flows to loft dust grains. Thus, low-mass planets may be consistent with well-defined and settled dust rings. Explicit simulations will be required to test this hypothesis.

In this work we adopt a high kinematic viscosity $\nu = 10^{-5} R_0^2 \Omega_{\rm K0}$. This value of viscosity, and the neglect of a corresponding dust diffusion (Youdin and Lithwick 2007), were purposely chosen to eliminate dust-lofting mechanisms other than the planet-induced meridional gas flows.

In real PPDs, the effective viscosity can be attributed to hydrodynamic turbulence, which provides additional particle stirring. For example, VSI can lead to weak turbulence ($\alpha \sim 10^{-4}$ for $h_{\rm g} = 0.05$; Manger et al. 2020), but is sufficient to carry small dust to the atmosphere (Stoll and Kley 2016), which may lead to even more significant dust 'puff-ups' if combined with planet stirring.

On the other hand, dust settling against VSI is sensitive to metallicity (e.g., Lin 2019), which is expected to increase around the outer gap edge as dust accumulates there. In order to study the combined effect of multiple mechanisms (e.g., VSI plus planet stirring), low viscosity (or inviscid) simulations are needed in future work, which also require much higher resolutions to resolve small-scale turbulent motions (Picogna et al. 2018; Manger et al. 2020).

3.4 Conclusions

In this chapter, we use 3D hydrodynamic simulations to study the dust kinematics in protoplanetary disks where a planet is present. Our main findings are:

1. Small, sub-mm-sized dust grains relatively well-coupled to the gas can be carried to higher disk elevations by the meridional flows around the gap edges caused by a gap-opening planet. In the case of a Saturn-mass planet, 100-μm-sized grains can be carried up to 1–2 gas scale-heights.

2. Grain size is the primary factor that affect the dust 'puff-up'. Larger ($\gtrsim$ mm-sized) grains can settle against the stirring by a Saturn-mass planet. While large planet masses produce stronger 'puff-ups', even weakly gap-opening planets can puff-up sub-mm-sized dust grains.

We conclude that dust grain sizes should exceed mm when attributing well-settled dust rings to gas-gap-opening planets. We thus caution that explicit 3D simulations cannot be replaced by 2D ones followed by a vertical expansion without taking into account the 'puff-up' by planet-induced meridional flows when studying the sharpness of the mm emission associated with gas gaps opened by planets. However, our results do not rule out the possibility that low-mass planets (e.g., super-Earths) may open dust gaps without perturbing the gas significantly, thereby allowing dust rings to settle.

Appendix A

GW Ori: Interactions Between a Triple-star System and its Circumtriple Disk in Action

A.1 ALMA ^{12}CO J=2-1 Zeroth-moment Map

Figure A.1 shows the ALMA zeroth-moment map of ^{12}CO $J = 2 - 1$ emission. The spiral-like structure at $\sim 0.75''$ to the northwest is likely due to cloud contamination, as reported by previous studies (Czekala et al. 2017; Fang et al. 2017).

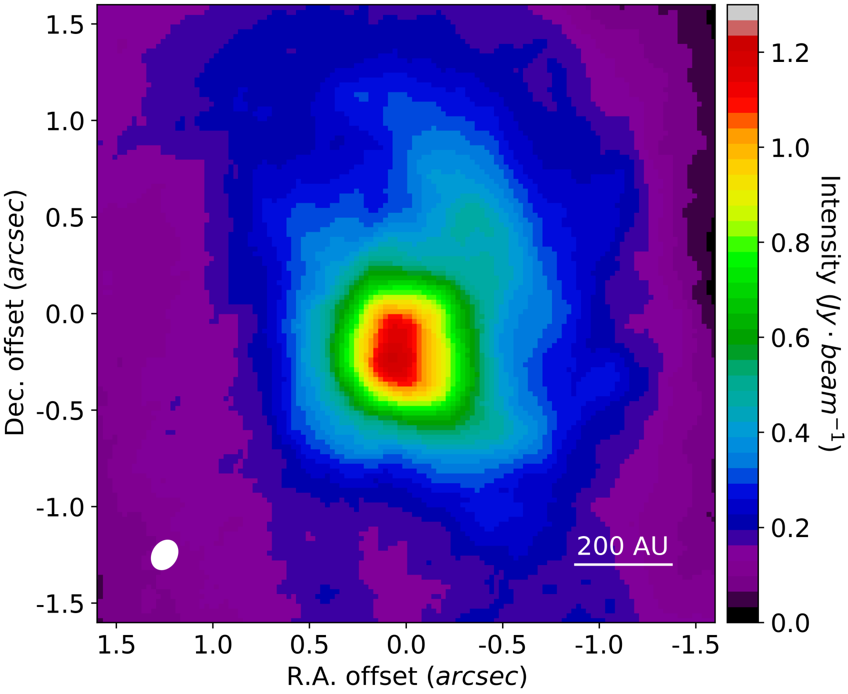

Figure A.1: The ALMA zeroth-moment map of ^{12}CO $J = 2 - 1$ emission.

A.2 the uv-plot and posterior distribution of dust modelling

Figure A.2 shows the *uv*-plot and posterior distribution of Model 3.

A.3 Equations for the Time-scale Analysis

A.3.1 Radial Communication Time-scale

For a disk around a binary system of separation a_b, its radial communication time-scale t_c can be estimated by Lubow and Martin (2018)

$$t_c \approx \frac{8}{5\Omega_b (h/r)_{\rm out}} \left(\frac{r_{\rm out}}{a_{\rm b}}\right)^{3/2} \tag{A.1}$$

where $r_{\rm out}$ is the outer radius within which the disk is in good radial communication, and $(h/r)_{\rm out}$ is the aspect ratio at $r_{\rm out}$, calculated based on the estimated temperature in the disk (Equation 2.2). The radial communication time-scale of the entire disk (i.e., $r_{\rm out} = 1300$ AU) is estimated to be ~ 0.06 Myr.

A.3.2 Nodal Precession Time-scale

If there is no radial communication in the disk, each part of the disk shall undergo differential precession with its local precession angular frequency $\omega_{\rm n,local}$ given by Smallwood et al. (2019)

$$\omega_{\rm n,local} = k \left(\frac{a_{\rm b}}{r}\right)^{7/2} \Omega_{\rm b}, \tag{A.2}$$

where

$$k = \frac{3}{4}\sqrt{1 + 3e_{\rm b}^2 - 4e_{\rm b}^4}\,\frac{M_1 M_2}{(M_1 + M_2)^2} \tag{A.3}$$

is a constant depending on the eccentricity of binary's orbit $e_{\rm b}$, and the primary and secondary mass of the binary M_1 and M_2. However, for a protoplanetary disk in the bending-wave regime, where radial communication is active and prompt, the disk parts at different radii shall undergo *global* precession with the angular frequency $\omega_{\rm n,global}$ given by Smallwood et al. (2019)

$$\omega_{\rm n,global} = k \left\langle \left(\frac{a_{\rm b}}{r}\right)^{7/2} \right\rangle \Omega_{\rm b}, \tag{A.4}$$

and

$$\left\langle \left(\frac{a_\mathrm{b}}{r}\right)^{7/2} \right\rangle = \frac{\int_{r_\mathrm{in}}^{r_\mathrm{out}} \Sigma r^3 \Omega (a_\mathrm{b}/r)^{7/2} \mathrm{d}r}{\int_{r_\mathrm{in}}^{r_\mathrm{out}} \Sigma r^3 \Omega \mathrm{d}r} \tag{A.5}$$

is the angular momentum weighted averaging term, in which $\Omega(r)$ is the angular frequency at a given radius r, $\Sigma(r)$ is the disk surface density with a radial dependence of $r^{-3/2}$, and r_in and r_out are inner and outer radius of the disk. Assuming $r_\mathrm{in} = 32$ AU and $r_\mathrm{out} = 1300$ AU, we take $t_\mathrm{n,global} = 2\pi \ / \ \omega_\mathrm{n,global}$ and estimate the global precession time-scale of the entire GW Ori disk to be ~ 0.83 Myr.

A.3.3 Alignment Time-scale

The alignment time-scale t_a is given by Lubow and Martin (2018) and Bate et al. (2000)

$$t_\mathrm{a} = \frac{(h/r)^2 \, \Omega_\mathrm{b}}{\alpha \, \omega_\mathrm{n}^2}, \tag{A.6}$$

where $\alpha = 0.01$, h/r is defined in Equation 2.6, and the angular frequency of global precession (Equation A.4) is used for ω_n.

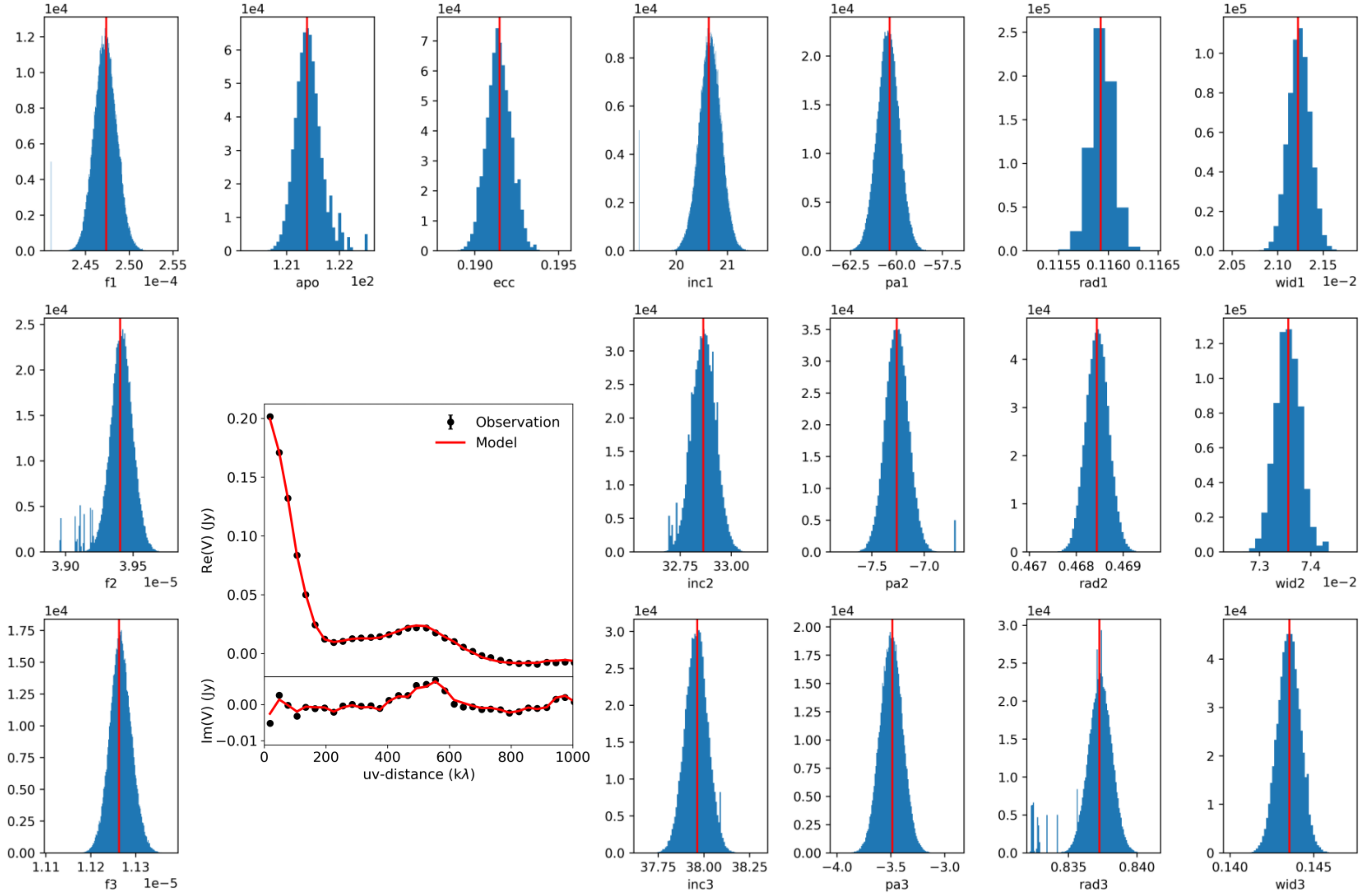

Figure A.2: The quality of MCMC parameter search for Model 3. The *uv*-visibility panel shows the *uv*-plot of both the ALMA observation and its best-fit model, with the upper panel for the real part of visibility and the lower panel for the imaginary part. The surrounding panels show the histograms of chains in the MCMC fitting. The best-fit value is taken from the 50th percentile of the distribution (vertical red line). And the negative and positive uncertainties are taken from 16th and 84th percentile, respectively. The seven columns are for the peak surface brightness, apoapsis angle (inner ring only), eccentricity (inner ring only), inclination, position angle, radius, and width, from left to right. And the three rows (top-down) are for the inner, middle, and outer ring. The units of parameters in the histograms are the same as those in Table 2.1c.

Appendix B

Planet-induced Meridional Flows of Sub-mm-sized Dust Grains in Protoplanetary Disks

B.1 Verification of the Terminal Velocity Approximation

To validate the terminal velocity approximation used to interpret our simulations, we here compare τ_s derived from Equation 3.24 in the vertical direction, namely $\tau_s = \rho(W_Z - V_Z)/(\partial P/\partial Z)$, with its prescribed definition in Equation 3.6. Results for the fiducial simulation derived from the two approaches are shown in Figure B.1 after taking a vertical and azimuthal average. The largest relative difference between the two results is $\sim 10\%$, therefore we conclude that the dust kinematics in our study is well-described by the terminal velocity approximation as stated in Eq. 3.24.

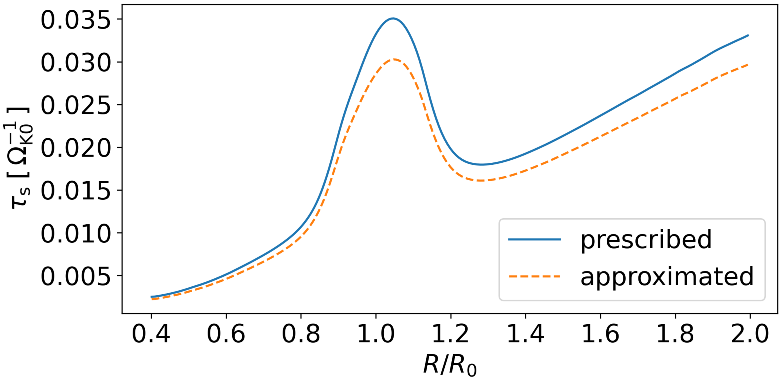

Figure B.1: Radial profiles of the particle stopping time. The values are azimuthally and vertically averaged (excluding azimuth within $\arcsin(3R_H/R_0)$ to the planet) and derived from Equation 3.6 (as prescribed in the simulations) and that inferred from the terminal velocity approximation (Equation 3.24) in the vertical direction, respectively. The fiducial simulation with a Saturn-mass planet and dust grains with $\mathrm{St}_0 = 10^{-3}$ is shown.

Bibliography

Sean M. Andrews, Jane Huang, Laura M. Pérez, Andrea Isella, Cornelis P. Dullemond, Nicolás T. Kurtovic, Viviana V. Guzmán, John M. Carpenter, David J. Wilner, Shangjia Zhang, Zhaohuan Zhu, Tilman Birnstiel, Xue-Ning Bai, Myriam Benisty, A. Meredith Hughes, Karin I. Öberg, and Luca Ricci. The Disk Substructures at High Angular Resolution Project (DSHARP). I. Motivation, Sample, Calibration, and Overview. *The Astrophysical Journal*, 869(2):L41, December 2018. ISSN 2041-8213. doi: 10.3847/2041-8213/aaf741. URL `https://iopscience.iop.org/article/10.3847/2041-8213/aaf741`.

Pawel Artymowicz and Stephen H. Lubow. Dynamics of Binary-Disk Interaction. I. Resonances and Disk Gap Sizes. *The Astrophysical Journal*, 421:651, February 1994. doi: 10.1086/173679. URL `https://ui.adsabs.harvard.edu/abs/1994ApJ...421..651A`.

Sayantan Auddy and Min-Kai Lin. A Machine Learning Model to Infer Planet Masses from Gaps Observed in Protoplanetary Disks. *The Astrophysical Journal*, 900(1):62, September 2020. ISSN 1538-4357. doi: 10.3847/1538-4357/aba95d. URL `https://iopscience.iop.org/article/10.3847/1538-4357/aba95d`.

Jaehan Bae, Richard P. Nelson, and Lee Hartmann. The Spiral Wave Instability Induced by a Giant Planet. I. Particle Stirring in the Inner Regions of Protoplanetary Disks. *The Astrophysical Journal*, 833(2):126, December 2016. ISSN 1538-4357. doi: 10.3847/1538-4357/833/2/126. URL `https://iopscience.iop.org/article/10.3847/1538-4357/833/2/126`.

Jaehan Bae, Zhaohuan Zhu, and Lee Hartmann. On the Formation of Multiple Concentric Rings and Gaps in Protoplanetary Disks. *The Astrophysical Journal*, 850(2):201, December 2017. ISSN 1538-4357. doi: 10.3847/1538-4357/aa9705. URL `https://iopscience.iop.org/article/10.3847/1538-4357/aa9705`.

Vanessa Bailey, Tiffany Meshkat, Megan Reiter, Katie Morzinski, Jared Males, Kate Y. L. Su, Philip M. Hinz, Matthew Kenworthy, Daniel Stark, Eric Mamajek, Runa Briguglio, Laird M. Close, Katherine B. Follette, Alfio Puglisi, Timothy Rodigas, Alycia J. Weinberger, and Marco Xompero. HD 106906 b: A Planetary-mass Companion Outside a Massive Debris Disk. *The Astrophysical Journal*, 780(1):L4, December 2013. ISSN 2041-8205, 2041-8213. doi: 10.1088/2041-8205/780/1/L4. URL `https://iopscience.iop.org/article/10.1088/2041-8205/780/1/L4`.

M. R. Bate, I. A. Bonnell, C. J. Clarke, S. H. Lubow, G. I. Ogilvie, J. E. Pringle, and C. A. Tout. Observational Implications of Precessing Protostellar Discs and Jets. *Monthly Notices of the Royal Astronomical Society*, 317(4):773–781, October 2000. ISSN 0035-8711, 1365-2966. doi: 10.1046/j.1365-8711.2000.03648.x. URL `https://academic.oup.com/mnras/article-lookup/doi/10.1046/j.1365-8711.2000.03648.x`.

Matthew R. Bate. Stellar, Brown Dwarf and Multiple Star Properties from a Radiation Hydrodynamical Simulation of Star Cluster Formation: Stellar and Multiple Star Properties. *Monthly Notices of the Royal Astronomical Society*, 419(4): 3115–3146, February 2012. ISSN 00358711. doi: 10.1111/j.1365-2966.2011.19955.x. URL `https://academic.oup.com/mnras/article-lookup/doi/10.1111/j.1365-2966.2011.19955.x`.

Matthew R Bate. On the Diversity and Statistical Properties of Protostellar Discs. *Monthly Notices of the Royal Astronomical Society*, 475(4):5618–5658, April 2018. ISSN 0035-8711, 1365-2966. doi: 10.1093/mnras/sty169. URL `https://academic.oup.com/mnras/article/475/4/5618/4822160`.

Steven V. W. Beckwith, Anneila I. Sargent, Rolf S. Chini, and Rolf Guesten. A Survey for Circumstellar Disks Around Young Stellar Objects. *The Astronomical Journal*, 99:924, March 1990. ISSN 00046256. doi: 10.1086/115385. URL `http://adsabs.harvard.edu/cgi-bin/bib_query?1990AJ.....99..924B`.

M. Benisty, A. Juhász, S. Facchini, P. Pinilla, J. de Boer, L. M. Pérez, M. Keppler, G. Muro-Arena, M. Villenave, S. Andrews, C. Dominik, C. P. Dullemond, A. Gallenne, A. Garufi, C. Ginski, and A. Isella. Shadows and Asymmetries in the T Tauri Disk HD 143006: Evidence for a Misaligned Inner Disk. *Astronomy & Astrophysics*, 619:A171, November 2018. ISSN 0004-6361, 1432-0746. doi: 10.1051/0004-6361/201833913. URL `https://www.aanda.org/10.1051/0004-6361/201833913`.

Pablo Benítez-Llambay and Frédéric S. Masset. FARGO3D: A New GPU-oriented MHD Code. *The Astrophysical Journal Supplement Series*, 223(1):11, March 2016. ISSN 1538-4365. doi: 10.3847/0067-0049/223/1/11. URL `https://iopscience.iop.org/article/10.3847/0067-0049/223/1/11`.

J.-P. Berger, J. D. Monnier, R. Millan-Gabet, S. Renard, E. Pedretti, W. Traub, C. Bechet, M. Benisty, N. Carleton, P. Haguenauer, P. Kern, P. Labeye, F. Longa, M. Lacasse, F. Malbet, K. Perraut, S. Ragland, P. Schloerb, P. A. Schuller, and E. Thiébaut. First Astronomical Unit Scale Image of the GW Orionis Triple System: Direct Detection of a New Stellar Companion. *Astronomy & Astrophysics*, 529:L1, May 2011. ISSN 0004-6361, 1432-0746. doi: 10.1051/0004-6361/201016219. URL `http://www.aanda.org/10.1051/0004-6361/201016219`.

Ian Bonnell and Pierre Bastien. Fragmentation of Elongated Cylindrical Clouds. V. Dependence of Mass Ratios on Initial Conditions. *The Astrophysical Journal*, 401: 654, December 1992. doi: 10.1086/172093. URL `https://ui.adsabs.harvard.edu/abs/1992ApJ...401..654B`.

Alice S Booth and John D Ilee. 13C17O Suggests Gravitational Instability in the HL Tau Disc. *Monthly Notices of the Royal Astronomical Society: Letters*, 493(1): L108–L113, March 2020. ISSN 1745-3925, 1745-3933. doi: 10.1093/mnrasl/slaa014. URL `https://academic.oup.com/mnrasl/article/493/1/L108/5715469`.

Simon Bruderer. Survival of Molecular Gas in Cavities of Transition Disks: I. CO. *Astronomy & Astrophysics*, 559:A46, November 2013. ISSN 0004-6361, 1432-0746. doi: 10.1051/0004-6361/201321171. URL `http://www.aanda.org/10.1051/0004-6361/201321171`.

F. Busetti, H. Beust, and C. Harley. Stability of Planets in Triple Star Systems. *Astronomy & Astrophysics*, 619:A91, November 2018. ISSN 0004-6361, 1432-0746. doi: 10.1051/0004-6361/201833097. URL `https://www.aanda.org/10.1051/0004-6361/201833097`.

Nuria Calvet, James Muzerolle, César Briceño, Jesus Hernández, Lee Hartmann, José Luis Saucedo, and Karl D. Gordon. The Mass Accretion Rates of Intermediate-mass T Tauri Stars. *The Astronomical Journal*, 128(3):1294–1318, September 2004. ISSN 0004-6256, 1538-3881. doi: 10.1086/422733. URL `https://iopscience.iop.org/article/10.1086/422733`.

S. Casassus, S. Marino, S. Pérez, P. Roman, A. Dunhill, P. J. Armitage, J. Cuadra, A. Wootten, G. van der Plas, L. Cieza, Victor Moral, V. Christiaens, and Matías Montesinos. Accretion Kinematics Through the Warped Transition Disk in HD 142527 from Resolved CO(6–5) Observations. *The Astrophysical Journal*, 811(2): 92, September 2015. ISSN 1538-4357. doi: 10.1088/0004-637X/811/2/92. URL `https://iopscience.iop.org/article/10.1088/0004-637X/811/2/92`.

Jhih-Wei Chen and Min-Kai Lin. Dusty Disc–planet Interaction with Dust-free Simulations. *Monthly Notices of the Royal Astronomical Society*, 478(2):2737–2752, August 2018. ISSN 0035-8711, 1365-2966. doi: 10.1093/mnras/sty1166. URL `https://academic.oup.com/mnras/article/478/2/2737/4992769`.

Ian Czekala, Sean M. Andrews, Guillermo Torres, Joseph E. Rodriguez, Eric L. N. Jensen, Keivan G. Stassun, David W. Latham, David J. Wilner, Michael A. Gully-Santiago, Konstantin N. Grankin, Michael B. Lund, Rudolf B. Kuhn, Daniel J. Stevens, Robert J. Siverd, David James, B. Scott Gaudi, Benjamin J. Shappee, and Thomas W.-S. Holoien. The Architecture of the GW Ori Young Triple-Star System and Its Disk: Dynamical Masses, Mutual Inclinations, and Recurrent Eclipses. *The Astrophysical Journal*, 851(2):132, December 2017. ISSN 1538-4357. doi: 10.3847/1538-4357/aa9be7. URL `https://iopscience.iop.org/article/10.3847/1538-4357/aa9be7`.

M. De Val-Borro, R. G. Edgar, P. Artymowicz, P. Ciecielag, P. Cresswell, G. D'Angelo, E. J. Delgado-Donate, G. Dirksen, S. Fromang, A. Gawryszczak, H. Klahr, W. Kley, W. Lyra, F. Masset, G. Mellema, R. P. Nelson, S.-J. Paardekooper, A. Peplinski, A. Pierens, T. Plewa, K. Rice, C. Schafer, and R. Speith. A Comparative Study of Disc-planet Interaction. *Monthly Notices of the Royal Astronomical Society*, 370(2):529–558, August 2006. ISSN 0035-8711, 1365-2966. doi: 10.1111/j.1365-2966.2006.10488.x. URL `https://academic.oup.com/mnras/article-lookup/doi/10.1111/j.1365-2966.2006.10488.x`.

Giovanni Dipierro and Guillaume Laibe. An Opening Criterion for Dust Gaps in Protoplanetary Discs. *Monthly Notices of the Royal Astronomical Society*, 469(2): 1932–1948, August 2017. ISSN 0035-8711, 1365-2966. doi: 10.1093/mnras/stx977. URL `https://academic.oup.com/mnras/article/469/2/1932/3752452`.

Giovanni Dipierro, Daniel Price, Guillaume Laibe, Kieran Hirsh, Alice Cerioli, and Giuseppe Lodato. On Planet Formation in HL Tau. *Monthly Notices of the*

Royal Astronomical Society: Letters, 453(1):L73–L77, October 2015. ISSN 1745-3925, 1745-3933. doi: 10.1093/mnrasl/slv105. URL `https://academic.oup.com/mnrasl/article-lookup/doi/10.1093/mnrasl/slv105`.

Ruobing Dong, Zhaohuan Zhu, and Barbara Whitney. Observational Signatures of Planets in Protoplanetary Disks. I. Gaps Opened by Single and Multiple Young Planets in Disks. *The Astrophysical Journal*, 809(1):93, August 2015. ISSN 1538-4357. doi: 10.1088/0004-637X/809/1/93. URL `https://iopscience.iop.org/article/10.1088/0004-637X/809/1/93`.

Ruobing Dong, Shengtai Li, Eugene Chiang, and Hui Li. Multiple Disk Gaps and Rings Generated by a Single Super-Earth. *The Astrophysical Journal*, 843(2):127, July 2017. ISSN 1538-4357. doi: 10.3847/1538-4357/aa72f2. URL `https://iopscience.iop.org/article/10.3847/1538-4357/aa72f2`.

Ruobing Dong, Shengtai Li, Eugene Chiang, and Hui Li. Multiple Disk Gaps and Rings Generated by a Single Super-Earth. II. Spacings, Depths, and Number of Gaps, with Application to Real Systems. *The Astrophysical Journal*, 866(2):110, October 2018a. ISSN 1538-4357. doi: 10.3847/1538-4357/aadadd. URL `https://iopscience.iop.org/article/10.3847/1538-4357/aadadd`.

Ruobing Dong, Sheng-yuan Liu, Josh Eisner, Sean Andrews, Jeffrey Fung, Zhaohuan Zhu, Eugene Chiang, Jun Hashimoto, Hauyu Baobab Liu, Simon Casassus, Thomas Esposito, Yasuhiro Hasegawa, Takayuki Muto, Yaroslav Pavlyuchenkov, David Wilner, Eiji Akiyama, Motohide Tamura, and John Wisniewski. The Eccentric Cavity, Triple Rings, Two-armed Spirals, and Double Clumps of the MWC 758 Disk. *The Astrophysical Journal*, 860(2):124, June 2018b. ISSN 1538-4357. doi: 10.3847/1538-4357/aac6cb. URL `https://iopscience.iop.org/article/10.3847/1538-4357/aac6cb`.

Ruobing Dong, Joan R. Najita, and Sean Brittain. Spiral Arms in Disks: Planets or Gravitational Instability? *The Astrophysical Journal*, 862(2):103, July 2018c. ISSN 1538-4357. doi: 10.3847/1538-4357/aaccfc. URL `https://iopscience.iop.org/article/10.3847/1538-4357/aaccfc`.

Ruobing Dong, Sheng-Yuan Liu, and Jeffrey Fung. Observational Signatures of Planets in Protoplanetary Disks: Planet-induced Line Broadening in Gaps. *The Astrophysical Journal*, 870(2):72, January 2019. ISSN 1538-4357. doi: 10.

3847/1538-4357/aaf38e. URL `https://iopscience.iop.org/article/10.3847/1538-4357/aaf38e`.

J. Drążkowska and Y. Alibert. Planetesimal Formation Starts at the Snow Line. *Astronomy & Astrophysics*, 608:A92, December 2017. ISSN 0004-6361, 1432-0746. doi: 10.1051/0004-6361/201731491. URL `http://www.aanda.org/10.1051/0004-6361/201731491`.

B. Dubrulle, G. Morfill, and M. Sterzik. The Dust Subdisk in the Protoplanetary Nebula. *Icarus*, 114(2):237–246, April 1995. doi: 10.1006/icar.1995.1058.

S. Facchini, M. Benisty, J. Bae, R. Loomis, L. Perez, M. Ansdell, S. Mayama, P. Pinilla, R. Teague, A. Isella, and A. Mann. Annular Substructures in the Transition Disks Around LkCa 15 and J1610. *Astronomy & Astrophysics*, 639:A121, July 2020. ISSN 0004-6361, 1432-0746. doi: 10.1051/0004-6361/202038027. URL `https://www.aanda.org/10.1051/0004-6361/202038027`.

Stefano Facchini, Attila Juhász, and Giuseppe Lodato. Signatures of Broken Protoplanetary Discs in Scattered Light and in Sub-millimetre Observations. *Monthly Notices of the Royal Astronomical Society*, 473(4):4459–4475, February 2018. ISSN 0035-8711, 1365-2966. doi: 10.1093/mnras/stx2523. URL `http://academic.oup.com/mnras/article/473/4/4459/4315947`.

M. Fang, A. Sicilia-Aguilar, V. Roccatagliata, D. Fedele, Th. Henning, C. Eiroa, and A. Müller. GW Orionis: Inner Disk Readjustments in a Triple System. *Astronomy & Astrophysics*, 570:A118, October 2014. ISSN 0004-6361, 1432-0746. doi: 10.1051/0004-6361/201424146. URL `http://www.aanda.org/10.1051/0004-6361/201424146`.

M. Fang, A. Sicilia-Aguilar, D. Wilner, Y. Wang, V. Roccatagliata, D. Fedele, and J. Z. Wang. Millimeter Observations of the Disk Around GW Orionis. *Astronomy & Astrophysics*, 603:A132, July 2017. ISSN 0004-6361, 1432-0746. doi: 10.1051/0004-6361/201628792. URL `http://www.aanda.org/10.1051/0004-6361/201628792`.

F. C. Fekel, Jr. The Properties of Close Multiple Stars. *The Astrophysical Journal*, 246:879, June 1981. ISSN 0004-637X, 1538-4357. doi: 10.1086/158981. URL `http://adsabs.harvard.edu/doi/10.1086/158981`.

Kevin M. Flaherty, A. Meredith Hughes, Sanaea C. Rose, Jacob B. Simon, Chunhua Qi, Sean M. Andrews, Ágnes Kóspál, David J. Wilner, Eugene Chiang, Philip J. Armitage, and Xue-ning Bai. A Three-Dimensional View of Turbulence: Constraints on Turbulent Motions in the HD 163296 Protoplanetary Disk Using DCO+. *The Astrophysical Journal*, 843(2):150, July 2017. ISSN 1538-4357. doi: 10.3847/1538-4357/aa79f9. URL `https://iopscience.iop.org/article/10.3847/1538-4357/aa79f9`.

Mario Flock, Richard P. Nelson, Neal J. Turner, Gesa H.-M. Bertrang, Carlos Carrasco-González, Thomas Henning, Wladimir Lyra, and Richard Teague. Radiation Hydrodynamical Turbulence in Protoplanetary Disks: Numerical Models and Observational Constraints. *The Astrophysical Journal*, 850(2):131, November 2017. ISSN 1538-4357. doi: 10.3847/1538-4357/aa943f. URL `https://iopscience.iop.org/article/10.3847/1538-4357/aa943f`.

Mario Flock, Neal J. Turner, Richard P. Nelson, Wladimir Lyra, Natascha Manger, and Hubert Klahr. Gas and Dust Dynamics in Starlight-heated Protoplanetary Disks. *The Astrophysical Journal*, 897(2):155, July 2020. ISSN 1538-4357. doi: 10.3847/1538-4357/ab9641. URL `https://iopscience.iop.org/article/10.3847/1538-4357/ab9641`.

Daniel Foreman-Mackey, David W. Hogg, Dustin Lang, and Jonathan Goodman. emcee : The MCMC Hammer. *Publications of the Astronomical Society of the Pacific*, 125(925):306–312, March 2013. ISSN 00046280, 15383873. doi: 10.1086/670067. URL `http://iopscience.iop.org/article/10.1086/670067`.

L. Fouchet, S. T. Maddison, J.-F. Gonzalez, and J. R. Murray. The Effect of a Planet on the Dust Distribution in a 3D Protoplanetary Disk. *Astronomy & Astrophysics*, 474(3):1037–1047, November 2007. ISSN 0004-6361, 1432-0746. doi: 10.1051/0004-6361:20077586. URL `http://www.aanda.org/10.1051/0004-6361:20077586`.

S. Fromang and J. Papaloizou. Dust Settling in Local Simulations of Turbulent Protoplanetary Disks. *Astronomy & Astrophysics*, 452(3):751–762, June 2006. ISSN 0004-6361, 1432-0746. doi: 10.1051/0004-6361:20054612. URL `http://www.aanda.org/10.1051/0004-6361:20054612`.

Jeffrey Fung and Eugene Chiang. Gap Opening in 3D: Single-planet Gaps. *The Astrophysical Journal*, 832(2):105, November 2016. ISSN 1538-4357. doi: 10.3847/0004-637X/832/2/105. URL `https://iopscience.iop.org/article/10.3847/0004-637X/832/2/105`.

Gaia Collaboration, A. G. A. Brown, A. Vallenari, T. Prusti, J. H. J. de Bruijne, C. Babusiaux, C. A. L. Bailer-Jones, M. Biermann, D. W. Evans, L. Eyer, F. Jansen, C. Jordi, S. A. Klioner, U. Lammers, L. Lindegren, X. Luri, F. Mignard, C. Panem, D. Pourbaix, S. Randich, P. Sartoretti, H. I. Siddiqui, C. Soubiran, F. van Leeuwen, N. A. Walton, F. Arenou, U. Bastian, M. Cropper, R. Drimmel, D. Katz, M. G. Lattanzi, J. Bakker, C. Cacciari, J. Castañeda, L. Chaoul, N. Cheek, F. De Angeli, C. Fabricius, R. Guerra, B. Holl, E. Masana, R. Messineo, N. Mowlavi, K. Nienartowicz, P. Panuzzo, J. Portell, M. Riello, G. M. Seabroke, P. Tanga, F. Thévenin, G. Gracia-Abril, G. Comoretto, M. Garcia-Reinaldos, D. Teyssier, M. Altmann, R. Andrae, M. Audard, I. Bellas-Velidis, K. Benson, J. Berthier, R. Blomme, P. Burgess, G. Busso, B. Carry, A. Cellino, G. Clementini, M. Clotet, O. Creevey, M. Davidson, J. De Ridder, L. Delchambre, A. Dell'Oro, C. Ducourant, J. Fernández-Hernández, M. Fouesneau, Y. Frémat, L. Galluccio, M. García-Torres, J. González-Núñez, J. J. González-Vidal, E. Gosset, L. P. Guy, J.-L. Halbwachs, N. C. Hambly, D. L. Harrison, J. Hernández, D. Hestroffer, S. T. Hodgkin, A. Hutton, G. Jasniewicz, A. Jean-Antoine-Piccolo, S. Jordan, A. J. Korn, A. Krone-Martins, A. C. Lanzafame, T. Lebzelter, W. Löffler, M. Manteiga, P. M. Marrese, J. M. Martín-Fleitas, A. Moitinho, A. Mora, K. Muinonen, J. Osinde, E. Pancino, T. Pauwels, J.-M. Petit, A. Recio-Blanco, P. J. Richards, L. Rimoldini, A. C. Robin, L. M. Sarro, C. Siopis, M. Smith, A. Sozzetti, M. Süveges, J. Torra, W. van Reeven, U. Abbas, A. Abreu Aramburu, S. Accart, C. Aerts, G. Altavilla, M. A. Álvarez, R. Alvarez, J. Alves, R. I. Anderson, A. H. Andrei, E. Anglada Varela, E. Antiche, T. Antoja, B. Arcay, T. L. Astraatmadja, N. Bach, S. G. Baker, L. Balaguer-Núñez, P. Balm, C. Barache, C. Barata, D. Barbato, F. Barblan, P. S. Barklem, D. Barrado, M. Barros, M. A. Barstow, S. Bartholomé Muñoz, J.-L. Bassilana, U. Becciani, M. Bellazzini, A. Berihuete, S. Bertone, L. Bianchi, O. Bienaymé, S. Blanco-Cuaresma, T. Boch, C. Boeche, A. Bombrun, R. Borrachero, D. Bossini, S. Bouquillon, G. Bourda, A. Bragaglia, L. Bramante, M. A. Breddels, A. Bressan, N. Brouillet, T. Brüsemeister, E. Brugaletta, B. Bucciarelli, A. Burlacu, D. Busonero, A. G. Butkevich,

R. Buzzi, E. Caffau, R. Cancelliere, G. Cannizzaro, T. Cantat-Gaudin, R. Carballo, T. Carlucci, J. M. Carrasco, L. Casamiquela, M. Castellani, A. Castro-Ginard, P. Charlot, L. Chemin, A. Chiavassa, G. Cocozza, G. Costigan, S. Cowell, F. Crifo, M. Crosta, C. Crowley, J. Cuypers†, C. Dafonte, Y. Damerdji, A. Dapergolas, P. David, M. David, P. de Laverny, F. De Luise, R. De March, D. de Martino, R. de Souza, A. de Torres, J. Debosscher, E. del Pozo, M. Delbo, A. Delgado, H. E. Delgado, P. Di Matteo, S. Diakite, C. Diener, E. Distefano, C. Dolding, P. Drazinos, J. Durán, B. Edvardsson, H. Enke, K. Eriksson, P. Esquej, G. Eynard Bontemps, C. Fabre, M. Fabrizio, S. Faigler, A. J. Falcão, M. Farràs Casas, L. Federici, G. Fedorets, P. Fernique, F. Figueras, F. Filippi, K. Findeisen, A. Fonti, E. Fraile, M. Fraser, B. Frézouls, M. Gai, S. Galleti, D. Garabato, F. García-Sedano, A. Garofalo, N. Garralda, A. Gavel, P. Gavras, J. Gerssen, R. Geyer, P. Giacobbe, G. Gilmore, S. Girona, G. Giuffrida, F. Glass, M. Gomes, M. Granvik, A. Gueguen, A. Guerrier, J. Guiraud, R. Gutiérrez-Sánchez, R. Haigron, D. Hatzidimitriou, M. Hauser, M. Haywood, U. Heiter, A. Helmi, J. Heu, T. Hilger, D. Hobbs, W. Hofmann, G. Holland, H. E. Huckle, A. Hypki, V. Icardi, K. Janßen, G. Jevardat de Fombelle, P. G. Jonker, Á. L. Juhász, F. Julbe, A. Karampelas, A. Kewley, J. Klar, A. Kochoska, R. Kohley, K. Kolenberg, M. Kontizas, E. Kontizas, S. E. Koposov, G. Kordopatis, Z. Kostrzewa-Rutkowska, P. Koubsky, S. Lambert, A. F. Lanza, Y. Lasne, J.-B. Lavigne, Y. Le Fustec, C. Le Poncin-Lafitte, Y. Lebreton, S. Leccia, N. Leclerc, I. Lecoeur-Taibi, H. Lenhardt, F. Leroux, S. Liao, E. Licata, H. E. P. Lindstrøm, T. A. Lister, E. Livanou, A. Lobel, M. López, S. Managau, R. G. Mann, G. Mantelet, O. Marchal, J. M. Marchant, M. Marconi, S. Marinoni, G. Marschalkó, D. J. Marshall, M. Martino, G. Marton, N. Mary, D. Massari, G. Matijevič, T. Mazeh, P. J. McMillan, S. Messina, D. Michalik, N. R. Millar, D. Molina, R. Molinaro, L. Molnár, P. Montegriffo, R. Mor, R. Morbidelli, T. Morel, D. Morris, A. F. Mulone, T. Muraveva, I. Musella, G. Nelemans, L. Nicastro, L. Noval, W. O'Mullane, C. Ordénovic, D. Ordóñez-Blanco, P. Osborne, C. Pagani, I. Pagano, F. Pailler, H. Palacin, L. Palaversa, A. Panahi, M. Pawlak, A. M. Piersimoni, F.-X. Pineau, E. Plachy, G. Plum, E. Poggio, E. Poujoulet, A. Prša, L. Pulone, E. Racero, S. Ragaini, N. Rambaux, M. Ramos-Lerate, S. Regibo, C. Reylé, F. Riclet, V. Ripepi, A. Riva, A. Rivard, G. Rixon, T. Roegiers, M. Roelens, M. Romero-Gómez, N. Rowell, F. Royer, L. Ruiz-Dern, G. Sadowski, T. Sagristà Sellés, J. Sahlmann, J. Salgado, E. Salguero, N. Sanna, T. Santana-Ros, M. Sarasso, H. Savietto, M. Schultheis, E. Sciacca, M. Segol,

J. C. Segovia, D. Ségransan, I-C. Shih, L. Siltala, A. F. Silva, R. L. Smart, K. W. Smith, E. Solano, F. Solitro, R. Sordo, S. Soria Nieto, J. Souchay, A. Spagna, F. Spoto, U. Stampa, I. A. Steele, H. Steidelmüller, C. A. Stephenson, H. Stoev, F. F. Suess, J. Surdej, L. Szabados, E. Szegedi-Elek, D. Tapiador, F. Taris, G. Tauran, M. B. Taylor, R. Teixeira, D. Terrett, P. Teyssandier, W. Thuillot, A. Titarenko, F. Torra Clotet, C. Turon, A. Ulla, E. Utrilla, S. Uzzi, M. Vaillant, G. Valentini, V. Valette, A. van Elteren, E. Van Hemelryck, M. van Leeuwen, M. Vaschetto, A. Vecchiato, J. Veljanoski, Y. Viala, D. Vicente, S. Vogt, C. von Essen, H. Voss, V. Votruba, S. Voutsinas, G. Walmsley, M. Weiler, O. Wertz, T. Wevers, Ł. Wyrzykowski, A. Yoldas, M. Žerjal, H. Ziaeepour, J. Zorec, S. Zschocke, S. Zucker, C. Zurbach, and T. Zwitter. GAIA Data Release 2: Summary of the Contents and Survey Properties. *Astronomy & Astrophysics*, 616:A1, August 2018. ISSN 0004-6361, 1432-0746. doi: 10.1051/0004-6361/201833051. URL https://www.aanda.org/10.1051/0004-6361/201833051.

J. Goodman and R. R. Rafikov. Planetary Torques as the Viscosity of Protoplanetary Disks. *The Astrophysical Journal*, 552:793–802, May 2001. doi: 10.1086/320572. URL https://iopscience-iop-org.ezproxy.library.uvic.ca/article/10.1086/320572/pdf.

S. Y. Haffert, A. J. Bohn, J. de Boer, I. A. G. Snellen, J. Brinchmann, J. H. Girard, C. U. Keller, and R. Bacon. Two Accreting Protoplanets Around the Young Star PDS 70. *Nature Astronomy*, 3:749–754, June 2019. doi: 10.1038/s41550-019-0780-5.

R. H. Hildebrand. The Determination of Cloud Masses and Dust Characteristics from Submillimetre Thermal Emission. *Quarterly Journal of the Royal Astronomical Society*, 24:267–282, September 1983. URL https://ui.adsabs.harvard.edu/abs/1983QJRAS..24..267H.

He-Feng Hsieh and Min-Kai Lin. Migrating Low-mass Planets in Inviscid Dusty Protoplanetary Discs. *Monthly Notices of the Royal Astronomical Society*, 497(2):2425–2441, September 2020. ISSN 0035-8711, 1365-2966. doi: 10.1093/mnras/staa2115. URL https://academic.oup.com/mnras/article/497/2/2425/5873675.

Xiao Hu, Zhaohuan Zhu, Satoshi Okuzumi, Xue-Ning Bai, Lile Wang, Kengo Tomida, and James M. Stone. Nonideal MHD Simulation of HL Tau Disk: Formation of Rings. *The Astrophysical Journal*, 885(1):36, October 2019. ISSN 1538-4357. doi: 10.3847/1538-4357/ab44cb. URL https://iopscience.iop.org/article/10.3847/1538-4357/ab44cb.

Jane Huang, Sean M. Andrews, Cornelis P. Dullemond, Andrea Isella, Laura M. Pérez, Viviana V. Guzmán, Karin I. Öberg, Zhaohuan Zhu, Shangjia Zhang, Xue-Ning Bai, Myriam Benisty, Tilman Birnstiel, John M. Carpenter, A. Meredith Hughes, Luca Ricci, Erik Weaver, and David J. Wilner. The Disk Substructures at High Angular Resolution Project (DSHARP). II. Characteristics of Annular Substructures. *The Astrophysical Journal*, 869(2):L42, December 2018. ISSN 2041-8213. doi: 10.3847/2041-8213/aaf740. URL https://iopscience.iop.org/article/10.3847/2041-8213/aaf740.

Jane Huang, Sean M. Andrews, Cornelis P. Dullemond, Karin I. Öberg, Chunhua Qi, Zhaohuan Zhu, Tilman Birnstiel, John M. Carpenter, Andrea Isella, Enrique Macías, Melissa K. McClure, Laura M. Pérez, Richard Teague, David J. Wilner, and Shangjia Zhang. A Multifrequency ALMA Characterization of Substructures in the GM Aur Protoplanetary Disk. *The Astrophysical Journal*, 891(1):48, March 2020. ISSN 1538-4357. doi: 10.3847/1538-4357/ab711e. URL https://iopscience.iop.org/article/10.3847/1538-4357/ab711e.

Emmanuel Jacquet, Steven Balbus, and Henrik Latter. On Linear Dust-gas Streaming Instabilities in Protoplanetary Discs: Linear Dust-gas Streaming Instabilities. *Monthly Notices of the Royal Astronomical Society*, 415(4):3591–3598, August 2011. ISSN 00358711. doi: 10.1111/j.1365-2966.2011.18971.x. URL https://academic.oup.com/mnras/article-lookup/doi/10.1111/j.1365-2966.2011.18971.x.

Sheng Jin, Shengtai Li, Andrea Isella, Hui Li, and Jianghui Ji. Modeling Dust Emission of HL Tau Disk Based on Planet–Disk Interactions. *The Astrophysical Journal*, 818(1):76, February 2016. ISSN 1538-4357. doi: 10.3847/0004-637X/818/1/76. URL https://iopscience.iop.org/article/10.3847/0004-637X/818/1/76.

Kazuhiro D. Kanagawa, Takayuki Muto, Hidekazu Tanaka, Takayuki Tanigawa, Taku Takeuchi, Takashi Tsukagoshi, and Munetake Momose. Mass Constraint for a Planet in a Protoplanetary Disk from the Gap Width. *Publications of the Astronomical Society of Japan*, 68(3):43, June 2016. ISSN 0004-6264, 2053-051X. doi: 10.1093/pasj/psw037. URL https://academic.oup.com/pasj/article-lookup/doi/10.1093/pasj/psw037.

Kazuhiro D. Kanagawa, Takahiro Ueda, Takayuki Muto, and Satoshi Okuzumi. Effect of Dust Radial Drift on Viscous Evolution of Gaseous Disk. *The Astrophysical Journal*, 844(2):142, August 2017. ISSN 1538-4357. doi: 10.3847/1538-4357/aa7ca1. URL `https://iopscience.iop.org/article/10.3847/1538-4357/aa7ca1`.

Akimasa Kataoka, Takayuki Muto, Munetake Momose, Takashi Tsukagoshi, and Cornelis P Dullemond. Grain Size Constraints on HL Tau with Polarization Signature. *The Astrophysical Journal*, 820(1):54, March 2016. ISSN 1538-4357. doi: 10.3847/0004-637X/820/1/54. URL `https://iopscience.iop.org/article/10.3847/0004-637X/820/1/54`.

Akimasa Kataoka, Takashi Tsukagoshi, Adriana Pohl, Takayuki Muto, Hiroshi Nagai, Ian W. Stephens, Kohji Tomisaka, and Munetake Momose. The Evidence of Radio Polarization Induced by the Radiative Grain Alignment and Self-scattering of Dust Grains in a Protoplanetary Disk. *The Astrophysical Journal*, 844(1):L5, July 2017. ISSN 2041-8213. doi: 10.3847/2041-8213/aa7e33. URL `https://iopscience.iop.org/article/10.3847/2041-8213/aa7e33`.

M. Keppler, M. Benisty, A. Müller, Th. Henning, R. van Boekel, F. Cantalloube, C. Ginski, R. G. van Holstein, A.-L. Maire, A. Pohl, M. Samland, H. Avenhaus, J.-L. Baudino, A. Boccaletti, J. de Boer, M. Bonnefoy, G. Chauvin, S. Desidera, M. Langlois, C. Lazzoni, G.-D. Marleau, C. Mordasini, N. Pawellek, T. Stolker, A. Vigan, A. Zurlo, T. Birnstiel, W. Brandner, M. Feldt, M. Flock, J. Girard, R. Gratton, J. Hagelberg, A. Isella, M. Janson, A. Juhasz, J. Kemmer, Q. Kral, A.-M. Lagrange, R. Launhardt, A. Matter, F. Ménard, J. Milli, P. Mollière, J. Olofsson, L. Pérez, P. Pinilla, C. Pinte, S. P. Quanz, T. Schmidt, S. Udry, Z. Wahhaj, J. P. Williams, E. Buenzli, M. Cudel, C. Dominik, R. Galicher, M. Kasper, J. Lannier, D. Mesa, D. Mouillet, S. Peretti, C. Perrot, G. Salter, E. Sissa, F. Wildi, L. Abe, J. Antichi, J.-C. Augereau, A. Baruffolo, P. Baudoz, A. Bazzon, J.-L. Beuzit, P. Blanchard, S. S. Brems, T. Buey, V. De Caprio, M. Carbillet, M. Carle, E. Cascone, A. Cheetham, R. Claudi, A. Costille, A. Delboulbé, K. Dohlen, D. Fantinel, P. Feautrier, T. Fusco, E. Giro, L. Gluck, C. Gry, N. Hubin, E. Hugot, M. Jaquet, D. Le Mignant, M. Llored, F. Madec, Y. Magnard, P. Martinez, D. Maurel, M. Meyer, O. Möller-Nilsson, T. Moulin, L. Mugnier, A. Origné, A. Pavlov, D. Perret, C. Petit, J. Pragt, P. Puget, P. Rabou, J. Ramos, F. Rigal, S. Rochat, R. Roelfsema, G. Rousset, A. Roux, B. Salasnich, J.-F. Sauvage, A. Sevin, C. Soenke, E. Stadler, M. Suarez, M. Turatto, and L. Weber. Discovery of a Planetary-mass Companion Within the Gap of the Transition Disk Around PDS 70. *Astronomy & Astrophysics*, 617:A44, September 2018. ISSN 0004-6361, 1432-0746. doi: 10.1051/0004-6361/201832957. URL `https://www.aanda.org/10.1051/0004-6361/201832957`.

Josef Koller, Hui Li, and Douglas N. C. Lin. Vortices in the Co-orbital Region of an Embedded Protoplanet. *The Astrophysical Journal*, 596(1):L91–L94, October 2003. ISSN 0004-637X, 1538-4357. doi: 10.1086/379032. URL `https://iopscience.iop.org/article/10.1086/379032`.

D. G. Korycansky and J. C. B. Papaloizou. A Method for Calculations of Nonlinear Shear Flow: Application to Formation of Giant Planets in the Solar Nebula. *The Astrophysical Journal Supplement Series*, 105:181, July 1996. doi: 10.1086/192311. URL `http://articles.adsabs.harvard.edu/pdf/1996ApJS..105..181K`.

Stefan Kraus, Alexander Kreplin, Alison K. Young, Matthew R. Bate, John D. Monnier, Tim J. Harries, Henning Avenhaus, Jacques Kluska, Anna S. E. Laws, Evan A. Rich, Matthew Willson, Alicia N. Aarnio, Fred C. Adams, Sean M. Andrews, Narsireddy Anugu, Jaehan Bae, Theo ten Brummelaar, Nuria Calvet, Michel Curé, Claire L. Davies, Jacob Ennis, Catherine Espaillat, Tyler Gardner, Lee Hartmann, Sasha Hinkley, Aaron Labdon, Cyprien Lanthermann, Jean-Baptiste LeBouquin, Gail H. Schaefer, Benjamin R. Setterholm, David Wilner, and Zhaohuan Zhu. A Triple-star System with a Misaligned and Warped Circumstellar Disk Shaped by Disk Tearing. *Science*, 369(6508):1233–1238, September 2020. ISSN 0036-8075, 1095-9203. doi: 10.1126/science.aba4633. URL `https://www.sciencemag.org/lookup/doi/10.1126/science.aba4633`.

Guillaume Laibe, Charles-Edouard Bréhier, and Maxime Lombart. On the Settling of Small Grains in Dusty Discs: Analysis and Formulae. *Monthly Notices of the Royal Astronomical Society*, 494(4):5134–5147, June 2020. ISSN 0035-8711, 1365-2966. doi: 10.1093/mnras/staa994. URL `https://academic.oup.com/mnras/article/494/4/5134/5829884`.

M. Lambrechts, A. Johansen, and A. Morbidelli. Separating Gas-giant and Ice-giant Planets by Halting Pebble Accretion. *Astronomy & Astrophysics*, 572:A35, December 2014. ISSN 0004-6361, 1432-0746. doi: 10.1051/0004-6361/201423814. URL `http://www.aanda.org/10.1051/0004-6361/201423814`.

H. Li, S. H. Lubow, S. Li, and D. N. C. Lin. Type I Planet Migration in Nearly Laminar Disks. *The Astrophysical Journal*, 690(1):L52–L55, January 2009. ISSN 0004-637X, 1538-4357. doi: 10.1088/0004-637X/690/1/L52. URL `https://iopscience.iop.org/article/10.1088/0004-637X/690/1/L52`.

Hui Li, Shengtai Li, Josef Koller, Burton B. Wendroff, Richard Liska, Chris M. Orban, Edison P. T. Liang, and Douglas N. C. Lin. Potential Vorticity Evolution of a Protoplanetary Disk with an Embedded Protoplanet. *The Astrophysical Journal*, 624(2):1003–1009, May 2005. ISSN 0004-637X, 1538-4357. doi: 10.1086/429367. URL `https://iopscience.iop.org/article/10.1086/429367`.

D. N. C. Lin and J. C. B. Papaloizou. On the Tidal Interaction Between Protostellar Disks and Companions. In *Protostars and Planets III*. January 1993. URL `http://articles.adsabs.harvard.edu/pdf/1993prpl.conf..749L`.

Min-Kai Lin. Dust Settling Against Hydrodynamic Turbulence in Protoplanetary Discs. *Monthly Notices of the Royal Astronomical Society*, 485(4):5221–5234, June 2019. ISSN 0035-8711, 1365-2966. doi: 10.1093/mnras/stz701. URL `https://academic.oup.com/mnras/article/485/4/5221/5374533`.

Min-Kai Lin and John C. B. Papaloizou. Type III Migration in a Low-viscosity Disc. *Monthly Notices of the Royal Astronomical Society*, April 2010. ISSN 00358711, 13652966. doi: 10.1111/j.1365-2966.2010.16560.x. URL `https://academic.oup.com/mnras/article-lookup/doi/10.1111/j.1365-2966.2010.16560.x`.

Min-Kai Lin and Andrew N. Youdin. A Thermodynamic View of Dusty Protoplanetary Disks. *The Astrophysical Journal*, 849(2):129, November 2017. ISSN 1538-4357. doi: 10.3847/1538-4357/aa92cd. URL `https://iopscience.iop.org/article/10.3847/1538-4357/aa92cd`.

Hauyu Baobab Liu. The Anomalously Low (Sub)Millimeter Spectral Indices of Some Protoplanetary Disks May be Explained by Dust Self-scattering. *The Astrophysical Journal*, 877(2):L22, May 2019. ISSN 2041-8213. doi: 10.3847/2041-8213/ab1f8e. URL `https://iopscience.iop.org/article/10.3847/2041-8213/ab1f8e`.

Giuseppe Lodato and Daniel J. Price. On the Diffusive Propagation of Warps in Thin Accretion Discs. *Monthly Notices of the Royal Astronomical Society*, March 2010. ISSN 00358711, 13652966. doi: 10.1111/j.1365-2966.2010.16526.

x. URL `https://academic.oup.com/mnras/article-lookup/doi/10.1111/j.1365-2966.2010.16526.x`.

Giuseppe Lodato, Giovanni Dipierro, Enrico Ragusa, Feng Long, Gregory J Herczeg, Ilaria Pascucci, Paola Pinilla, Carlo F Manara, Marco Tazzari, Yao Liu, Gijs D Mulders, Daniel Harsono, Yann Boehler, François Ménard, Doug Johnstone, Colette Salyk, Gerrit van der Plas, Sylvie Cabrit, Suzan Edwards, William J Fischer, Nathan Hendler, Brunella Nisini, Elisabetta Rigliaco, Henning Avenhaus, Andrea Banzatti, and Michael Gully-Santiago. The Newborn Planet Population Emerging from Ring-like Structures in Discs. *Monthly Notices of the Royal Astronomical Society*, 486(1):453–461, June 2019. ISSN 0035-8711, 1365-2966. doi: 10.1093/mnras/stz913. URL `https://academic.oup.com/mnras/article/486/1/453/5423333`.

Feng Long, Paola Pinilla, Gregory J. Herczeg, Daniel Harsono, Giovanni Dipierro, Ilaria Pascucci, Nathan Hendler, Marco Tazzari, Enrico Ragusa, Colette Salyk, Suzan Edwards, Giuseppe Lodato, Gerrit van de Plas, Doug Johnstone, Yao Liu, Yann Boehler, Sylvie Cabrit, Carlo F. Manara, Francois Menard, Gijs D. Mulders, Brunella Nisini, William J. Fischer, Elisabetta Rigliaco, Andrea Banzatti, Henning Avenhaus, and Michael Gully-Santiago. Gaps and Rings in an ALMA Survey of Disks in the Taurus Star-forming Region. *The Astrophysical Journal*, 869(1):17, December 2018. ISSN 1538-4357. doi: 10.3847/1538-4357/aae8e1. URL `https://iopscience.iop.org/article/10.3847/1538-4357/aae8e1`.

Francesco Lovascio and Sijme-Jan Paardekooper. Dynamics of Dusty Vortices – I. Extensions and Limitations of the Terminal Velocity Approximation. *Monthly Notices of the Royal Astronomical Society*, 488(4):5290–5299, October 2019. ISSN 0035-8711, 1365-2966. doi: 10.1093/mnras/stz2035. URL `https://academic.oup.com/mnras/article/488/4/5290/5541075`.

Stephen H. Lubow. A Model for Tidally Driven Eccentric Instabilities in Fluid Disks. *The Astrophysical Journal*, 381:259, November 1991. ISSN 0004-637X, 1538-4357. doi: 10.1086/170647. URL `http://adsabs.harvard.edu/doi/10.1086/170647`.

Stephen H. Lubow and Rebecca G. Martin. Linear Analysis of the Evolution of Nearly Polar Low-mass Circumbinary Discs. *Monthly Notices of the Royal Astronomical Society*, 473(3):3733–3746, January 2018. ISSN 0035-8711, 1365-2966. doi: 10.1093/mnras/stx2643. URL `http://academic.oup.com/mnras/article/473/3/3733/4443208`.

D. Lynden-Bell and J. E. Pringle. The Evolution of Viscous Discs and the Origin of the Nebular Variables. *Monthly Notices of the Royal Astronomical Society*, 168(3):603–637, September 1974. doi: 10.1093/mnras/168.3.603. URL https://academic-oup-com.ezproxy.library.uvic.ca/mnras/article/168/3/603/990948.

Natascha Manger, Hubert Klahr, Wilhelm Kley, and Mario Flock. High Resolution Parameter Study of the Vertical Shear Instability. *arXiv:2008.09006 [astro-ph]*, August 2020. URL http://arxiv.org/abs/2008.09006. arXiv: 2008.09006.

S. Marino, S. Perez, and S. Casassus. Shadows Cast by a Warp in the HD 142527 Protoplanetary Disk. *The Astrophysical Journal*, 798(2):L44, January 2015. ISSN 2041-8213. doi: 10.1088/2041-8205/798/2/L44. URL https://iopscience.iop.org/article/10.1088/2041-8205/798/2/L44.

Rebecca G. Martin and Stephen H. Lubow. Polar Alignment of a Protoplanetary Disk Around an Eccentric Binary. *The Astrophysical Journal*, 835(2):L28, January 2017. ISSN 2041-8213. doi: 10.3847/2041-8213/835/2/L28. URL https://iopscience.iop.org/article/10.3847/2041-8213/835/2/L28.

Rebecca G Martin and Stephen H Lubow. Polar Alignment of a Protoplanetary Disc Around an Eccentric Binary – III. Effect of Disc Mass. *Monthly Notices of the Royal Astronomical Society*, 490(1):1332–1349, November 2019. ISSN 0035-8711, 1365-2966. doi: 10.1093/mnras/stz2670. URL https://academic.oup.com/mnras/article/490/1/1332/5573825.

F. Masset. FARGO: A Fast Eulerian Transport Algorithm for Differentiallyrotating Disks. *Astronomy and Astrophysics Supplement Series*, 141(1):165–173, January 2000. ISSN 0365-0138, 1286-4846. doi: 10.1051/aas:2000116. URL http://aas.aanda.org/10.1051/aas:2000116.

Robert D. Mathieu, Fred C. Adams, and David W. Latham. The T Tauri Spectroscopic Binary GW Orionis. *The Astronomical Journal*, 101:2184, June 1991. ISSN 00046256. doi: 10.1086/115841. URL http://adsabs.harvard.edu/cgi-bin/bib_query?1991AJ....101.2184M.

M. K. McClure, E. A. Bergin, L. I. Cleeves, E. F. van Dishoeck, G. A. Blake, N. J. Evans II, J. D. Green, Th. Henning, K. I. Öberg, K. M. Pontoppidan, and

C. Salyk. Mass Measurements in Protoplanetary Disks from Hydrogen Deuteride. *The Astrophysical Journal*, 831(2):167, November 2016. ISSN 1538-4357. doi: 10.3847/0004-637X/831/2/167. URL https://iopscience.iop.org/article/10.3847/0004-637X/831/2/167.

J. P. McMullin, B. Waters, D. Schiebel, W. Young, and K. Golap. CASA architecture and applications. In R. A. Shaw, F. Hill, and D. J. Bell, editors, *Astronomical data analysis software and systems XVI*, volume 376 of *Astronomical society of the pacific conference series*, page 127. 2007.

Colin P McNally, Richard P Nelson, Sijme-Jan Paardekooper, and Pablo Benítez-Llambay. Migrating Super-Earths in Low-viscosity Discs: Unveiling the Roles of Feedback, Vortices, and Laminar Accretion Flows. *Monthly Notices of the Royal Astronomical Society*, 484(1):728–748, March 2019. ISSN 0035-8711, 1365-2966. doi: 10.1093/mnras/stz023. URL https://academic.oup.com/mnras/article/484/1/728/5274149.

Farzana Meru, Giovanni P Rosotti, Richard A Booth, Pooneh Nazari, and Cathie J Clarke. Is the ring inside or outside the planet?: the effect of planet migration on dust rings. *Monthly Notices of the Royal Astronomical Society*, 482(3):3678–3695, January 2019. ISSN 0035-8711, 1365-2966. doi: 10.1093/mnras/sty2847. URL https://academic.oup.com/mnras/article/482/3/3678/5144226.

A. Morbidelli, J. Szulágyi, A. Crida, Elena Lega, Bertram Bitsch, Takayuki Tanigawa, and Kazuhiro Kanagawa. Meridional Circulation of Gas into Gaps Opened by Giant Planets in Three-Dimensional Low-Viscosity Disks. *Icarus*, 232:266, April 2014. doi: 10.1016/j.icarus.2014.01.010.

Yoshitsugu Nakagawa, Kiyoshi Nakazawa, and Chushiro Hayashi. Growth and Sedimentation of Dust Grains in the Primordial Solar Nebula. *Icarus*, 45:12, March 1981. doi: 10.1016/0019-1035(81)90018-X.

Richard P. Nelson, Oliver Gressel, and Orkan M. Umurhan. Linear and Non-linear Evolution of the Vertical Shear Instability in Accretion Discs. *Monthly Notices of the Royal Astronomical Society*, 435(3):2610–2632, November 2013. ISSN 1365-2966, 0035-8711. doi: 10.1093/mnras/stt1475. URL http://academic.oup.com/mnras/article/435/3/2610/1031890/Linear-and-nonlinear-evolution-of-the-vertical.

C. J. Nixon, A. R. King, and J. E. Pringle. The Final Parsec Problem: Aligning a Binary with an External Accretion Disc: Disc-binary Alignment. *Monthly Notices of the Royal Astronomical Society: Letters*, 417(1):L66–L69, October 2011. ISSN 17453925. doi: 10.1111/j.1745-3933.2011.01121.x. URL `https://academic.oup.com/mnrasl/article-lookup/doi/10.1111/j.1745-3933.2011.01121.x`.

Chris Nixon, Andrew King, and Daniel Price. Tearing up the Disc: Misaligned Accretion on to a Binary. *Monthly Notices of the Royal Astronomical Society*, 434(3):1946–1954, September 2013. ISSN 0035-8711, 1365-2966. doi: 10.1093/mnras/stt1136. URL `http://academic.oup.com/mnras/article/434/3/1946/1031485/Tearing-up-the-disc-misaligned-accretion-on-to-a`.

S.-J. Paardekooper and G. Mellema. Planets Opening Dust Gaps in Gas Disks. *Astronomy & Astrophysics*, 425(1):L9–L12, October 2004. ISSN 0004-6361, 1432-0746. doi: 10.1051/0004-6361:200400053. URL `http://www.aanda.org/10.1051/0004-6361:200400053`.

S.-J. Paardekooper and G. Mellema. Dust Flow in Gas Disks in the Presence of Embedded Planets. *Astronomy & Astrophysics*, 453(3):1129–1140, July 2006. ISSN 0004-6361, 1432-0746. doi: 10.1051/0004-6361:20054449. URL `http://www.aanda.org/10.1051/0004-6361:20054449`.

J. C. B. Papaloizou, R. P. Nelson, and F. Masset. Orbital Eccentricity Growth Through Disc-companion Tidal Interaction. *Astronomy & Astrophysics*, 366(1):263–275, January 2001. ISSN 0004-6361, 1432-0746. doi: 10.1051/0004-6361:20000011. URL `http://www.aanda.org/10.1051/0004-6361:20000011`.

Giovanni Picogna, Moritz H. R. Stoll, and Wilhelm Kley. Particle Accretion Onto Planets in Discs with Hydrodynamic Turbulence. *Astronomy & Astrophysics*, 616:A116, August 2018. ISSN 0004-6361, 1432-0746. doi: 10.1051/0004-6361/201732523. URL `https://www.aanda.org/10.1051/0004-6361/201732523`.

P. Pinilla, A. Pohl, S. M. Stammler, and T. Birnstiel. Dust Density Distribution and Imaging Analysis of Different Ice Lines in Protoplanetary Disks. *The Astrophysical Journal*, 845(1):68, August 2017. ISSN 1538-4357. doi: 10.3847/1538-4357/aa7edb. URL `https://iopscience.iop.org/article/10.3847/1538-4357/aa7edb`.

C. Pinte, W. R. F. Dent, F. Ménard, A. Hales, T. Hill, P. Cortes, and I. de Gregorio-Monsalvo. Dust and Gas in the Disk of HL Tauri: Surface Density, Dust Settling, and Dust-to-Gas Ratio. *The Astrophysical Journal*, 816(1):25, January 2016. ISSN 1538-4357. doi: 10.3847/0004-637X/816/1/25. URL `https://iopscience.iop.org/article/10.3847/0004-637X/816/1/25`.

C. Pinte, D. J. Price, F. Ménard, G. Duchêne, V. Christiaens, S. M. Andrews, J. Huang, T. Hill, G. van der Plas, L. M. Perez, A. Isella, Y. Boehler, W. R. F. Dent, D. Mentiplay, and R. A. Loomis. Nine Localized Deviations from Keplerian Rotation in the DSHARP Circumstellar Disks: Kinematic Evidence for Protoplanets Carving the Gaps. *The Astrophysical Journal*, 890(1):L9, February 2020. ISSN 2041-8213. doi: 10.3847/2041-8213/ab6dda. URL `https://iopscience.iop.org/article/10.3847/2041-8213/ab6dda`.

James B. Pollack, Olenka Hubickyj, Peter Bodenheimer, Jack J. Lissauer, Morris Podolak, and Yuval Greenzweig. Formation of the Giant Planets by Concurrent Accretion of Solids and Gas. *Icarus*, 124(1):62–85, November 1996. ISSN 00191035. doi: 10.1006/icar.1996.0190. URL `https://linkinghub.elsevier.com/retrieve/pii/S0019103596901906`.

Daniel J. Price and Christoph Federrath. A Comparison Between Grid and Particle Methods on the Statistics of Driven, Supersonic, Isothermal Turbulence: Supersonic Turbulence: Grid Versus Sph. *Monthly Notices of the Royal Astronomical Society*, pages no–no, June 2010. ISSN 00358711, 13652966. doi: 10.1111/j.1365-2966.2010.16810.x. URL `https://academic.oup.com/mnras/article-lookup/doi/10.1111/j.1365-2966.2010.16810.x`.

Daniel J. Price and Guillaume Laibe. A Fast and Explicit Algorithm for Simulating the Dynamics of Small Dust Grains with Smoothed Particle Hydrodynamics. *Monthly Notices of the Royal Astronomical Society*, 451(1):813–826, July 2015. ISSN 1365-2966, 0035-8711. doi: 10.1093/mnras/stv996. URL `http://academic.oup.com/mnras/article/451/1/813/1380873/A-fast-and-explicit-algorithm-for-simulating-the`.

Daniel J. Price, James Wurster, Terrence S. Tricco, Chris Nixon, Stéven Toupin, Alex Pettitt, Conrad Chan, Daniel Mentiplay, Guillaume Laibe, Simon Glover, Clare Dobbs, Rebecca Nealon, David Liptai, Hauke Worpel, Clément Bonnerot, Giovanni Dipierro, Giulia Ballabio, Enrico Ragusa, Christoph Federrath, Roberto Iaconi, Thomas Reichardt, Duncan Forgan, Mark Hutchison, Thomas Constantino, Ben Ayliffe, Kieran Hirsh, and Giuseppe Lodato. PHANTOM: A Smoothed Particle Hydrodynamics and Magnetohydrodynamics Code for Astrophysics. *Publications of the Astronomical Society of Australia*, 35:e031, 2018. ISSN 1323-3580, 1448-6083. doi: 10.1017/pasa.2018.25. URL `https://www.cambridge.org/core/product/identifier/S1323358018000255/type/journal_article`.

Laura M. Pérez, Myriam Benisty, Sean M. Andrews, Andrea Isella, Cornelis P. Dullemond, Jane Huang, Nicolás T. Kurtovic, Viviana V. Guzmán, Zhaohuan Zhu, Tilman Birnstiel, Shangjia Zhang, John M. Carpenter, David J. Wilner, Luca Ricci, Xue-Ning Bai, Erik Weaver, and Karin I. Öberg. The Disk Substructures at High Angular Resolution Project (DSHARP). X. Multiple Rings, a Misaligned Inner Disk, and a Bright Arc in the Disk around the T Tauri star HD 143006. *The Astrophysical Journal*, 869(2):L50, December 2018. ISSN 2041-8213. doi: 10.3847/2041-8213/aaf745. URL `https://iopscience.iop.org/article/10.3847/2041-8213/aaf745`.

Katherine A. Rosenfeld, Eugene Chiang, and Sean M. Andrews. Fast Radial Flows in Transition Disk Holes. *The Astrophysical Journal*, 782(2):62, January 2014. ISSN 0004-637X, 1538-4357. doi: 10.1088/0004-637X/782/2/62. URL `https://iopscience.iop.org/article/10.1088/0004-637X/782/2/62`.

Giovanni P. Rosotti, Attila Juhasz, Richard A. Booth, and Cathie J. Clarke. The Minimum Mass of Detectable Planets in Protoplanetary Discs and the Derivation of Planetary Masses from High-resolution Observations. *Monthly Notices of the Royal Astronomical Society*, 459(3):2790–2805, July 2016. ISSN 0035-8711, 1365-2966. doi: 10.1093/mnras/stw691. URL `https://academic.oup.com/mnras/article-lookup/doi/10.1093/mnras/stw691`.

N. I. Shakura and R. A. Sunyaev. Reprint of 1973A&A....24..337S. Black Holes in Binary Systems. Observational Appearance. *Astronomy & Astrophysics*, 500:33–51, June 1973. URL `https://ui.adsabs.harvard.edu/abs/1973A&A....24..337S`.

Jeremy L Smallwood, Stephen H Lubow, Alessia Franchini, and Rebecca G Martin. Alignment of a Circumbinary Disc Around an Eccentric Binary with Application to KH 15D. *Monthly Notices of the Royal Astronomical Society*, 486(2):2919–2932, June 2019. ISSN 0035-8711, 1365-2966. doi: 10.1093/mnras/stz994. URL `https://academic.oup.com/mnras/article/486/2/2919/5437693`.

Moritz H. R. Stoll and Wilhelm Kley. Particle Dynamics in Discs with Turbulence Generated by the Vertical Shear Instability. *Astronomy & Astrophysics*, 594:A57, October 2016. ISSN 0004-6361, 1432-0746. doi: 10.1051/0004-6361/201527716. URL `http://www.aanda.org/10.1051/0004-6361/201527716`.

J. Szulágyi, A. Morbidelli, A. Crida, and F. Masset. Accretion of Jupiter-mass Planets in the Limit of Vanishing Viscosity. *The Astrophysical Journal*, 782(2):65, January 2014. ISSN 0004-637X, 1538-4357. doi: 10.1088/0004-637X/782/2/65. URL `https://iopscience.iop.org/article/10.1088/0004-637X/782/2/65`.

Taku Takeuchi and D. N. C. Lin. Radial Flow of Dust Particles in Accretion Disks. *The Astrophysical Journal*, 581(2):1344–1355, December 2002. ISSN 0004-637X, 1538-4357. doi: 10.1086/344437. URL `https://iopscience.iop.org/article/10.1086/344437`.

Marco Tazzari, Frederik Beaujean, and Leonardo Testi. GALARIO: A GPU Accelerated Library for Analysing Radio Interferometer Observations. *Monthly Notices of the Royal Astronomical Society*, 476(4):4527–4542, June 2018. ISSN 0035-8711, 1365-2966. doi: 10.1093/mnras/sty409. URL `https://academic.oup.com/mnras/article/476/4/4527/4867987`.

Richard Teague, Jaehan Bae, and Edwin A. Bergin. Meridional Flows in the Disk Around a Young Star. *Nature*, 574(7778):378–381, October 2019. ISSN 0028-0836, 1476-4687. doi: 10.1038/s41586-019-1642-0. URL `http://www.nature.com/articles/s41586-019-1642-0`.

Claudia Toci, Giuseppe Lodato, Davide Fedele, Leonardo Testi, and Christophe Pinte. Long-lived Dust Rings Around HD 169142. *The Astrophysical Journal*, 888(1):L4, January 2020. ISSN 2041-8213. doi: 10.3847/2041-8213/ab5c87. URL `https://iopscience.iop.org/article/10.3847/2041-8213/ab5c87`.

N. van der Marel, E. F. van Dishoeck, S. Bruderer, T. Birnstiel, P. Pinilla, C. P. Dullemond, T. A. van Kempen, M. Schmalzl, J. M. Brown, G. J. Herczeg, G. S. Mathews, and V. Geers. A Major Asymmetric Dust Trap in a Transition Disk. *Science*, 340(6137):1199–1202, June 2013. ISSN 0036-8075, 1095-9203. doi: 10.1126/science.1236770. URL `https://www.sciencemag.org/lookup/doi/10.1126/science.1236770`.

Nienke van der Marel, Ruobing Dong, James di Francesco, Jonathan P. Williams, and John Tobin. Protoplanetary Disk Rings and Gaps across Ages and Luminosities. *The Astrophysical Journal*, 872(1):112, February 2019. ISSN 1538-4357. doi: 10.3847/1538-4357/aafd31. URL `https://iopscience.iop.org/article/10.3847/1538-4357/aafd31`.

Catherine Walsh, Cail Daley, Stefano Facchini, and Attila Juhász. CO Emission Tracing a Warp or Radial Flow Within 100 AU in the HD 100546 Protoplanetary Disk. *Astronomy & Astrophysics*, 607:A114, November 2017. ISSN 0004-6361, 1432-0746. doi: 10.1051/0004-6361/201731334. URL `http://www.aanda.org/10.1051/0004-6361/201731334`.

Philipp Weber, Sebastián Pérez, Pablo Benítez-Llambay, Oliver Gressel, Simon Casassus, and Leonardo Krapp. Predicting the Observational Signature of Migrating Neptune-sized Planets in Low-viscosity Disks. *The Astrophysical Journal*, 884(2):178, October 2019. ISSN 1538-4357. doi: 10.3847/1538-4357/ab412f. URL `https://iopscience.iop.org/article/10.3847/1538-4357/ab412f`.

S. J. Weidenschilling. Aerodynamics of Solid Bodies in the Solar Nebula. *Monthly Notices of the Royal Astronomical Society*, 180(2):57–70, September 1977. ISSN 0035-8711, 1365-2966. doi: 10.1093/mnras/180.2.57. URL `https://academic.oup.com/mnras/article-lookup/doi/10.1093/mnras/180.2.57`.

F. L. Whipple. On Certain Aerodynamic Processes for Asteroids and Comets. In *From Plasma to Planet*, page 211. January 1972. URL `http://articles.adsabs.harvard.edu/pdf/1972fpp..conf..211W`.

Chao-Chin Yang and Zhaohuan Zhu. Morphological Signatures Induced by Dust Back Reaction in Discs with an Embedded Planet. *Monthly Notices of the Royal Astronomical Society*, page stz3232, November 2019. ISSN 0035-8711, 1365-2966. doi: 10.1093/mnras/stz3232. URL `https://academic.oup.com/mnras/advance-article/doi/10.1093/mnras/stz3232/5632129`.

Andrew N. Youdin and Jeremy Goodman. Streaming Instabilities in Protoplanetary Disks. *The Astrophysical Journal*, 620(1):459–469, February 2005. ISSN 0004-637X, 1538-4357. doi: 10.1086/426895. URL `https://iopscience.iop.org/article/10.1086/426895`.

Andrew N. Youdin and Yoram Lithwick. Particle Stirring in Turbulent Gas Disks: Including Orbital Oscillations. *Icarus*, 192(2):588–604, December 2007. ISSN 00191035. doi: 10.1016/j.icarus.2007.07.012. URL `https://linkinghub.elsevier.com/retrieve/pii/S0019103507003181`.

J. J. Zanazzi and Dong Lai. Inclination Evolution of Protoplanetary Discs Around Eccentric Binaries. *Monthly Notices of the Royal Astronomical Society*, 473(1): 603–615, January 2018. ISSN 0035-8711, 1365-2966. doi: 10.1093/mnras/stx2375. URL `https://academic.oup.com/mnras/article/473/1/603/4157814`.

Ke Zhang, Geoffrey A. Blake, and Edwin A. Bergin. Evidence of Fast Pebble Growth Near Condensation Fronts in the HL Tau Protoplanetary Disk. *The Astrophysical Journal*, 806(1):L7, June 2015. ISSN 2041-8213. doi: 10.1088/2041-8205/806/1/L7. URL `https://iopscience.iop.org/article/10.1088/2041-8205/806/1/L7`.

Shangjia Zhang and Zhaohuan Zhu. The Effects of Disc Self-gravity and Radiative Cooling on the Formation of Gaps and Spirals by Young Planets. *Monthly Notices of the Royal Astronomical Society*, 493(2):2287–2305, April 2020. ISSN 0035-8711, 1365-2966. doi: 10.1093/mnras/staa404. URL `https://academic.oup.com/mnras/article/493/2/2287/5733178`.

Shangjia Zhang, Zhaohuan Zhu, Jane Huang, Viviana V. Guzmán, Sean M. Andrews, Tilman Birnstiel, Cornelis P. Dullemond, John M. Carpenter, Andrea Isella, Laura M. Pérez, Myriam Benisty, David J. Wilner, Clément Baruteau, Xue-Ning Bai, and Luca Ricci. The Disk Substructures at High Angular Resolution Project (DSHARP). VII. The Planet–Disk Interactions Interpretation. *The Astrophysical Journal*, 869(2):L47, December 2018. ISSN 2041-8213. doi: 10.3847/2041-8213/aaf744. URL `https://iopscience.iop.org/article/10.3847/2041-8213/aaf744`.

Zhaohuan Zhu, James M. Stone, Roman R. Rafikov, and Xue-ning Bai. Particle Concentration at Planet-induced Gap Edges and Vortices. I. Inviscid Three-dimensional Hydro Disks. *The Astrophysical Journal*, 785(2):122, April 2014. ISSN 0004-637X, 1538-4357. doi: 10.1088/0004-637X/785/2/122. URL `https://iopscience.iop.org/article/10.1088/0004-637X/785/2/122`.

Zhaohuan Zhu, James M. Stone, and Xue-Ning Bai. Dust Transport in MRI Turbulent Disks: Ideal and Non-ideal MHD with Ambipolar Diffusion. *The Astrophysical*

Journal, 801(2):81, March 2015. ISSN 1538-4357. doi: 10.1088/0004-637X/801/2/81. URL https://iopscience.iop.org/article/10.1088/0004-637X/801/2/81.

Zhaohuan Zhu, Shangjia Zhang, Yan-Fei Jiang, Akimasa Kataoka, Tilman Birnstiel, Cornelis P. Dullemond, Sean M. Andrews, Jane Huang, Laura M. Pérez, John M. Carpenter, Xue-Ning Bai, David J. Wilner, and Luca Ricci. One Solution to the Mass Budget Problem for Planet Formation: Optically Thick Disks with Dust Scattering. *The Astrophysical Journal*, 877(2):L18, May 2019. ISSN 2041-8213. doi: 10.3847/2041-8213/ab1f8c. URL https://iopscience.iop.org/article/10.3847/2041-8213/ab1f8c.